Two-Dimensional Wavenumber Spectra on the Horizontal Submesoscale and Vertical Finescale

ANDA VLADOIU,[a] REN-CHIEH LIEN,[a] AND ERIC KUNZE[b]

[a] *Applied Physics Laboratory, University of Washington, Seattle, Washington*
[b] *NorthWest Research Associates, Seattle, Washington*

(Manuscript received 29 May 2021, in final form 25 April 2022)

ABSTRACT: Horizontal and vertical wavenumbers (k_x, k_z) immediately below the Ozmidov wavenumber $(N^3/\varepsilon)^{1/2}$ are spectrally distinct from both isotropic turbulence (k_x, $k_z > 1$ cpm) and internal waves as described by the Garrett–Munk (GM) model spectrum ($k_z < 0.1$ cpm). A towed CTD chain, augmented with concurrent Electromagnetic Autonomous Profiling Explorer (EM-APEX) profiling float microstructure measurements and shipboard ADCP surveys, are used to characterize 2D wavenumber (k_x, k_z) spectra of isopycnal slope, vertical strain, and isopycnal salinity gradient on horizontal wavelengths from 50 m to 250 km and vertical wavelengths of 2–48 m. For $k_z < 0.1$ cpm, 2D spectra of isopycnal slope and vertical strain resemble GM. Integrated over the other wavenumber, the isopycnal slope 1D k_x spectrum exhibits a roughly +1/3 slope for $k_x > 3 \times 10^{-3}$ cpm, and the vertical strain 1D k_z spectrum a −1 slope for $k_z > 0.1$ cpm, consistent with previous 1D measurements, numerical simulations, and anisotropic stratified turbulence theory. Isopycnal salinity gradient 1D k_x spectra have a +1 slope for $k_x > 2 \times 10^{-3}$ cpm, consistent with nonlocal stirring. Turbulent diapycnal diffusivities inferred in the (i) internal wave subrange using a vertical strain-based finescale parameterization are consistent with those inferred from finescale horizonal wavenumber spectra of (ii) isopycnal slope and (iii) isopycnal salinity gradients using Batchelor model spectra. This suggests that horizontal submesoscale and vertical finescale subranges participate in bridging the forward cascade between weakly nonlinear internal waves and isotropic turbulence, as hypothesized by anisotropic turbulence theory.

KEYWORDS: Internal waves; Mixing; Small scale processes; Turbulence

1. Introduction

In the stratified ocean interior away from boundaries, internal wave breaking is the primary source of isotropic turbulence and diapycnal mixing (e.g., Kunze 2017). However, there is an intermediate wavenumber subrange extending 1–2 decades in vertical wavenumber k_z and several decades in horizontal wavenumber k_x below the Ozmidov (1965) wavenumber $k_O \sim \mathcal{O}(1\text{–}10)$ cpm (wavelengths $\lambda \sim 0.1\text{–}1$ m) that is spectrally distinct from both isotropic turbulence ($k_z, k_x > k_O$) and internal gravity waves ($k_z < 0.1$ cpm) as described by the Garrett and Munk (1979) model spectrum, suggesting different dynamics apply. The Ozmidov (1965) wavenumber $k_O = (N^3/\varepsilon)^{1/2}$ is the lower bound wavenumber for isotropic turbulence, where ε is turbulent kinetic energy dissipation rate and N buoyancy frequency.

Vertical wavenumber k_z spectra of vertical shear and strain in the finescale subrange $k_{z_c} < k_z < k_O$ exhibit a −1 spectral slope (Gregg 1977; Dewan 1979; Gargett et al. 1981; Dewan and Good 1986; Smith et al. 1987; Fritts et al. 1988; Gregg et al. 1993; Dewan 1997), where the observed roll-off wavenumber $k_{z_c} \sim 0.1$ cpm (vertical wavelengths $\lambda_z \sim 10$ m). This differs from both the flat or slightly blue (positive slope) spectra below k_{z_c} where weakly nonlinear internal waves are thought to dominate, and the +1/3 slope of gradient spectra for isotropic turbulence above the Ozmidov wavenumber k_O (Fig. 1b).

Submesoscale horizontal wavenumber k_x spectra for horizontal temperature gradient or isopycnal slope (Katz 1973; Marmorino et al. 1985; Samelson and Paulson 1988) are flat for 100 m $< \lambda_x <$ 100 km. However, McKean and Ewart (1974) identified a +1/3 gradient spectral slope horizontal wavenumber subrange extending several decades below the Ozmidov wavenumber k_O (Nastrom and Gage 1985; Klymak and Moum 2007; Sheen et al. 2009; Holbrook et al. 2013; Falder et al. 2016; Fortin et al. 2016), similar to that of isotropic turbulence (Fig. 1a). Moreover, the spectral level for isopycnal slope exhibits the same dependence on turbulent kinetic energy dissipation rate ε as in isotropic turbulence (Klymak and Moum 2007), implying a turbulent energy cascade to dissipation at wavenumbers well below k_O.

If quasigeostrophic (QG) turbulence was the sole lateral stirring mechanism in the ocean, horizontal wavenumber spectra for passive tracer gradients, such as spice or salinity anomalies on isopycnals, would have +1 spectral slopes on length scales smaller than the Rossby deformation radius (NH/f for quasigeostrophy and $\int Ndz/f$ for surface quasigeostrophy, where f is the Coriolis frequency) due to nonlocal stirring (Batchelor 1959; Scott 2006; Smith and Ferrari 2009). However, numerical simulations and measurements find submesoscale spectral slopes for isopycnal salinity gradients ranging from −1 to +1 over horizontal wavenumbers $10^{-5} < k_x < 10^{-3}$ cpm (Capet et al. 2008a,b; Molemaker et al. 2010; Cole and Rudnick 2012; Callies and Ferrari 2013; Klymak et al. 2015; Jaeger et al. 2020),

Denotes content that is immediately available upon publication as open access.

Corresponding author: Anda Vladoiu, avladoiu@apl.uw.edu

DOI: 10.1175/JPO-D-21-0111.1

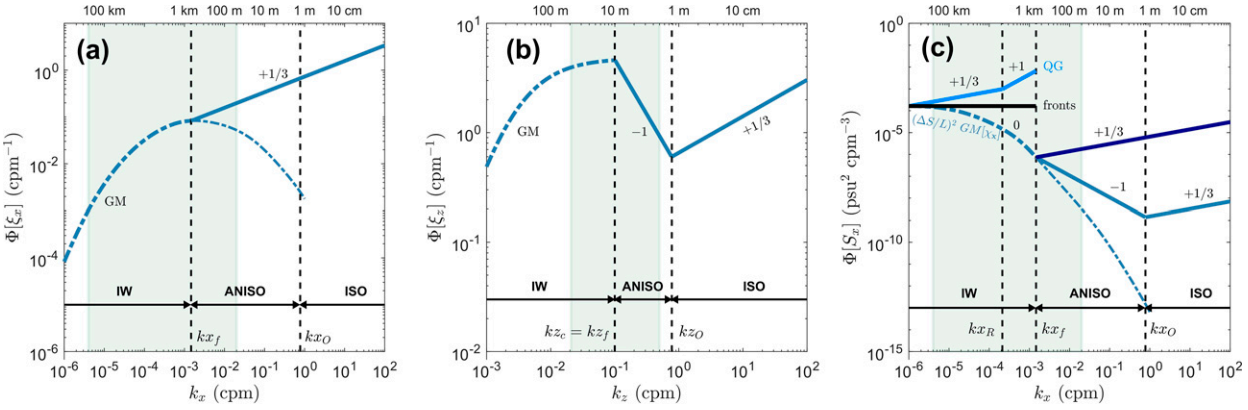

FIG. 1. Schematics of horizontal wavenumber spectra for (a) isopycnal slope ξ_x and (c) isopycnal salinity gradient S_x, and vertical wavenumber spectra for (b) vertical strain ξ_z. Theoretical spectral slopes in wavenumber ranges of GM internal gravity waves (IW, appendix C), anisotropic stratified turbulence (ANISO), and isotropic turbulence (ISO) are labeled, with spectral slopes indicated where relevant. Anisotropic turbulence is bound by the horizontal Coriolis wavenumber $k_{x_f} = (f^3/\varepsilon)^{1/2}$ and the Ozmidov wavenumber $k_O = (N^3/\varepsilon)^{1/2}$ in horizontal wavenumber and vertical Coriolis wavenumber $k_{z_f} = (fN^2/\varepsilon)^{1/2}$ and k_O in vertical wavenumber, where mean measured $N = 9.6 \times 10^{-3}$ s^{-1}, $f = 8 \times 10^{-5}$ s^{-1}, $\varepsilon = 6 \times 10^{-9}$ W kg^{-1}, and $k_{z_f} \sim$ canonical internal wave vertical cutoff wavenumber $k_{z_c} \sim 0.1$ cpm (Gargett et al. 1981) were used. Isotropic turbulence lies above the Ozmidov wavenumber. Panel (c) displays the predicted +1/3 spectral slopes for surface quasigeostrophy and +1 slope for subsurface quasigeostrophy (light blue), the flat spectrum for frontogenesis (black), normalized GM IW spectrum for horizontal strain χ_x (dash–dot), and predicted anisotropic turbulence −1 spectral slope (blue), as well as the predicted +1/3 slope for isotropic turbulence horizontal shear (dark blue). Green shading spans the wavenumber ranges resolved by the towed CTD chain measurements in this study.

signifying that other straining processes contribute to the tracer anomaly cascade, reddening tracer gradient spectra from a +1 QG spectral form (Fig. 1c). Possible processes include reversible but substantial internal wave horizontal strain (Kunze et al. 2015), frontogenesis, and anisotropic stratified turbulence (Kunze 2019).

While both internal waves and turbulence have been well studied spectrally and dynamically with observations, theory, and numerical modeling, the intermediate finescale vertical subrange $k_{z_c} < k_z < k_O$ is not well understood. Nonlinear kinematics, potential-vorticity-carrying fine structure (e.g., balanced vortical motions), double-diffusively-driven thermohaline intrusions, nonlinear internal waves, and anisotropic stratified turbulence have all been proposed to explain this intermediate subrange. It is challenging to study this subrange observationally because it requires separating weak signals from stronger internal wave fluctuations at larger scales, and theoretically because of its inherent nonlinearity. In the following, the vertical wavenumber subrange $k_{z_c} < k_z < k_O$ will be referred to as the *vertical finescale* or *anisotropic stratified turbulence* subrange, although other dynamics may apply, under the assumption that nonlinear turbulence with horizontal shears exceeding f (Ro > 1) overcomes internal waves and controls time scales in this subrange (Kunze 2019). Lower vertical wavenumbers $k_z < k_{z_c}$ are thought to be dominated by weakly nonlinear internal waves and balanced motions. Higher wavenumbers $k_z > k_O$ are dominated by strongly nonlinear isotropic turbulence. The corresponding horizontal wavenumber band $\sim 0.1(f/N)$ cpm $< k_x < k_O$, assuming Burger number Bu $= [Nk_x/(fk_z)]^2 \sim 1$ at k_{z_c}, will be referred to as the *horizontal submesoscale* or *anisotropic stratified turbulence* subrange.

The processes contributing to the $k_x^{+1/3}$ horizontal wavenumber subrange in isopycnal slope, the broad range of horizonal wavenumber spectral shapes for isopycnal tracer gradient, and the k_z^{-1} vertical wavenumber subrange in vertical shear and strain have been interpreted as anisotropic stratified turbulence (Riley and Lindborg 2008; Kunze 2019). Recent numerical modeling (Billant and Chomaz 2000, 2001; Waite and Bartello 2004; Lindborg 2005, 2006; Brethouwer et al. 2007) and observations (Lindborg and Cho 2000; Sheen et al. 2009; Klymak and Moum 2007; Fortin et al. 2016; Falder et al. 2016; Poje et al. 2017) suggest that anisotropic turbulence participates in a forward energy cascade at horizontal wavenumbers below the Ozmidov wavenumber k_O. Kunze (2019) equated this forward energy cascade rate with the turbulent dissipation rate ε and argued that anisotropic turbulence fed into isotropic turbulence.

Anisotropic turbulence is characterized by vertical shears $\sim \mathcal{O}(N)$ (Billant and Chomaz 2001; Riley and DeBruynkops 2003) and horizontal shears exceeding f (Lindborg 2006; Galperin et al. 2021). Using dimensional scaling arguments, Kunze (2019) formulated an anisotropic stratified turbulence spectral model that reproduces the observed k_z^{-1} vertical wavenumber subrange of vertical strain and shear, and the $k_x^{+1/3}$ horizontal wavenumber subrange of isopycnal slope (Fig. 1). In this spectral model, the lower horizontal and vertical wavenumber bounds for the anisotropic stratified turbulence subrange are horizontal and vertical Coriolis wavenumbers $(f^3/\varepsilon)^{1/2}$ and $(fN^2/\varepsilon)^{1/2}$, respectively. The horizontal Coriolis wavenumber marks the transition to turbulent horizontal shears exceeding f (Ro > 1) and where nonlinear horizontal momentum terms exceed linear terms. The vertical Coriolis wavenumber appears to correspond to the internal wave upper-bound roll-off vertical wavenumber k_{z_c} (Gargett et al. 1981). The upper bound for the anisotropic turbulence subrange is the Ozmidov wavenumber $k_O = (N^3/\varepsilon)^{1/2}$, marking

the transition to isotropic turbulence and shears exceeding N. The lower horizontal wavenumber bound for anisotropic stratified turbulence has not been observationally identified and will be discussed in this study. Likewise, the role of finescale processes in the forward energy and passive tracer cascades has not been confirmed observationally and will be examined here.

Previous measurements of the submesoscale and finescale subranges have been mostly 1D either in the horizontal or vertical. In this study, 2D measurements from a towed CTD (TCTD) chain spanning wavelengths (wavenumbers) $\lambda_x \sim 50$ m–250 km ($4 \times 10^{-6} < k_x < 2 \times 10^{-2}$ cpm) and $\lambda_z = 2$–48 m ($2 \times 10^{-2} < k_z < 0.5$ cpm), that is, straddling the vertical roll-off wavenumber ~0.1 cpm, are investigated. This study will 1) examine 2D horizontal and vertical wavenumber spectral properties for isopycnal slope, vertical strain and isopycnal salinity gradient, 2) discuss the relevance of the vertical strain k_z^{-1} vertical wavenumber subrange and isopycnal slope $k_x^{+1/3}$ horizontal wavenumber subrange for anisotropic stratified turbulence, 3) compare predicted properties of internal waves and anisotropic stratified turbulence with observed spectra, and 4) quantify the role of finescale processes in the energy and tracer variance cascades.

Section 2 outlines the data and methods. Section 3 presents the background hydrography, as well as frequency spectra. Sections 4–6 describe 2D and 1D spectra for isopycnal slope, vertical strain, and isopycnal salinity gradient. Section 7 compares diapycnal diffusivities inferred from the finescale strain parameterization (Polzin et al. 1995; Gregg et al. 2003) with those inferred from anisotropic stratified turbulence scaling (Batchelor 1959; Klymak and Moum 2007). Significant correlation of these independent estimates suggests that energy transfers occur from internal waves to isotropic turbulence through the intermediate anisotropic turbulence subrange. In other words, internal waves, anisotropic turbulence, and isotropic turbulence form a bucket brigade across wavenumber in the forward energy cascade to eventual dissipation. Last, section 8 provides a summary of the results, the interpretation of which is discussed further in section 9.

2. Experiment, data, and methods

a. Experiment

The measurements were collected during July 2018 in the upper 200 m of the eastern North Pacific (Fig. 2) on the edge of the California Current system off Baja California, a region of strong compensated temperature–salinity variability and moderate density contrasts, where intense mesoscale and submesoscale variability are well documented (e.g., Flament et al. 1985; Chereskin et al. 2000). Data presented here were collected with a TCTD chain and Electromagnetic Autonomous Profiling Explorer (EM-APEX) floats.

b. Towed CTD chain

The TCTD chain is a 200-m-long armored coax sea cable terminated with a V-fin depressor. The cable was mounted with 56 Sea-Bird Scientific SBE37 MicroCATs, sampling temperature, conductivity, and pressure every 12 s. A mounting system was designed to allow MicroCATs to swing freely on the cable. Fairings were added along the entire cable to reduce drag. MicroCAT data were transmitted to the deck in near–real time through an inductive cable during the survey to allow in situ analysis and water-mass tracking.

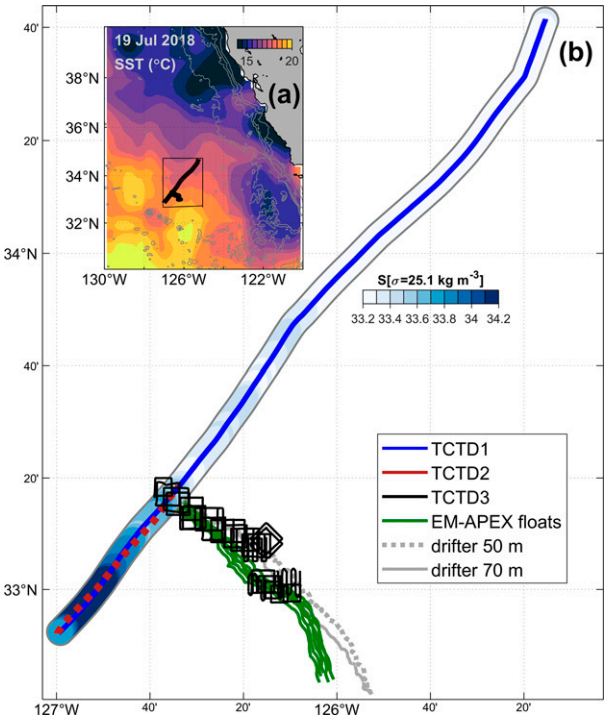

FIG. 2. (a) Map of AVHRR sea surface temperature (SST) (color contour inset) on 19 July 2018 with towed CTD chain (TCTD) survey ship track (thick black lines within the inset's black rectangle) and ETOPOP2v2 bathymetry contours every 1000 m (thin gray). (b) Expansion of the black rectangle in (a) showing TCTD1 (blue line), TCTD2 (red dotted line), and TCTD3 (black lines) surveys. Blue shading bracketing the TCTD1 line illustrates salinity on isopycnal $\sigma = 25$ kg m^{-3}. Green curves are trajectories of six EM-APEX floats, while dotted and solid gray curves trajectories of two surface drifters with drogues at 50- and 70-m depths, respectively.

The temperature resolution of the MicroCATs is 10^{-4}°C and salinity resolution 10^{-3} psu. Forty-eight of the MicroCATs were distributed at 1.5-m intervals along the cable to span the targeted 69–117-m depth aperture within the pycnocline. Six MicroCATs at 15-m intervals were mounted above the targeted depth window, and two MicroCATs at 11- and 25-m intervals below. Because of the tow angle due to cable drag, the actual depth separation between sensors in the targeted depth window is ~1 m.

Towed at ~2 m s^{-1}, TCTD chain measurements have a horizontal resolution of ~25 m, resolving fluctuations with horizontal wavelengths > 50 m. Space–time aliasing is minimal (appendix A), so that fluctuations of TCTD measurements are interpreted as spatial variability. TCTD sampling patterns (Fig. 2b) include

- one 260-km, 36-h-long section along a straight northeast–southwest line (TCTD1);

- one 60-km, 8-h-long section backtracking TCTD1 along a straight southwest–northeast line (TCTD2); and
- an ensemble of 136 7-km, 1-h-long sections with 120 sections in 30 box patterns and 16 sections in radiator patterns (TCTD3).

MicroCAT conductivity time series were despiked using an iterative method similar to that provided by the Rockland Scientific ODAS (Ocean Dissipation Acquisition System) processing software (Douglas and Lueck 2015). The signal was high-pass filtered and smoothed with a low-pass zero-phase filter, then compared to a local standard deviation computed by high-pass filtering in order to identify spikes. Identified spikes and their two adjacent data points were replaced with the mean value of the neighboring points inferred from the low-pass filter to minimize bias from unipolar pulses. Spikes account for less than 0.5% of the data.

c. EM-APEX floats

During the TCTD3 surveys, two drifters were drogued to 50- and 70-m depths to follow water movement in the pycnocline. Six EM-APEX floats (Sanford et al. 1985, 2005) equipped with dual FP07 thermistors were used to compute turbulent thermal variance dissipation rate χ by integrating the microscale temperature-gradient spectrum beyond the Batchelor roll-off wavenumber $(\varepsilon/\nu/\kappa_T^2)^{1/4}$, and infer turbulent kinetic energy dissipation rates $\varepsilon = \chi N^2/(2\Gamma\langle T_z\rangle^2)$ and thermal diffusivities $K_T = \chi/(2\langle T_z\rangle^2)$ (Lien et al. 2016). Floats also measured finescale horizontal velocity (u, v), temperature T, salinity S, and pressure. The floats profiled repeatedly in the upper 200 m with ~1-km horizontal and 1-h temporal resolution, while moving with the depth-mean flow. Vertical resolutions are 1, 2.6, and 7 m for χ, (T, S), and (u, v), respectively. Uncertainty in EM-APEX float horizontal currents is 0.015 m s^{-1}. The floats moved coherently with the drifters with little dispersion. TCTD3 surveyed around float and surface-drifter trajectories with additional guidance from the T–S properties of the near-real-time TCTD measurements (Fig. 2b).

d. Estimation of 1D and 2D wavenumber spectra

1) Spatial transformation of TCTD data

The TCTD measurements were converted to time series of latitude, longitude, and pressure using shipboard GPS positions, then interpolated onto a regular alongtrack horizontal grid with $\delta x = 25$ m and vertical grid with $\delta z = 1$ m for computation of 2D wavenumber spectra. The interpolation is performed using measured pressure, placement of individual sensors along the cable, distances of CTD sensors from shipboard ADCP, and ship and water current speeds. Details of this projection are described in appendix B. Correcting for water motion relative to Earth does not impact the spectra but is included for completeness.

2) Estimates of vertical isopycnal displacement

Gridded TCTD-measured potential density σ is depth-sorted to remove overturns in 6.7% of the data. For each (x, z) section, sorted σ is averaged over time at each 1-m depth grid level $z_{\overline{\sigma}}$ to obtain section-averaged density profiles $\overline{\sigma}(z)$. Vertical displacements of $\overline{\sigma}$ are computed as

$$\xi(x, z_{\overline{\sigma}}) = z(\overline{\sigma}) - z_{\overline{\sigma}}. \tag{1}$$

Displacements ξ are computed for isopycnals fluctuating within the ~69–117-m depth-average window with ~1-m vertical resolution.

3) Estimates of 1D and 2D spectrum of isopycnal slope

The 1D horizontal wavenumber spectra of isopycnal displacement $\Phi[\xi](k_x)$ are computed for each depth $z_{\overline{\sigma}}$. Horizontal wavenumber spectra for isopycnal slope were computed as $\Phi[\xi_x](k_x) = (2\pi k_x)^2\Phi[\xi](k_x)$, where the alongtrack horizontal wavenumber k_x is in cycles per meter (cpm).

For the 2D wavenumber spectra, resolved and larger-scale spatial contributions are separated. The vertical isopycnal displacements $\xi(x, z_{\overline{\sigma}})$ are decomposed into the depth-mean $\overline{\xi}^{z_{\overline{\sigma}}}(x)$, section-mean $\overline{\xi}^{x}(z_{\overline{\sigma}})$, 2D mean $\overline{\xi}^{xz_{\overline{\sigma}}}$, and resolved perturbation $\xi'(x, z_{\overline{\sigma}})$ as

$$\xi(x, z_{\overline{\sigma}}) = \xi'(x, z_{\overline{\sigma}}) + \overline{\xi}^{x}(z_{\overline{\sigma}}) + \overline{\xi}^{z_{\overline{\sigma}}}(x) + \overline{\xi}^{xz_{\overline{\sigma}}}, \tag{2}$$

where overbars indicate averages over the superscript dimension and $\xi'(x, z_{\overline{\sigma}})$ is used to compute the 2D (k_x, k_z) spectrum. Vertical means $\overline{\xi}^{z_{\overline{\sigma}}}(x)$ represent horizontal variations with vertical scales longer than 48 m, primarily dominated by low- and intermediate-mode internal waves. Horizontal means $\overline{\xi}^{x}(z_{\overline{\sigma}})$ are small. They do not include unresolved horizontal scales longer than the section length because displacements are computed relative to the section-mean density profile.

The 2D horizontal and vertical wavenumber spectra $\Phi[\xi'](k_x, k_z)$ and 1D horizontal wavenumber spectra $\Phi[\overline{\xi}^{z_{\overline{\sigma}}}](k_x)$ for each section are computed after applying 2D and 1D single sinusoidal tapers, respectively (Riedel and Sidorenko 1995).

4) Estimates of 1D and 2D spectrum of vertical strain

Vertical strain ξ_z is computed as

$$\xi_z(x, z_{\overline{\sigma}}) = \frac{\partial(z - z_{\overline{\sigma}})}{\partial z_{\overline{\sigma}}}, \tag{3}$$

where $\partial z_{\overline{\sigma}}$ and ∂z are the thickness between two isopycnals at the reference state and at x, respectively. This is identical to the definition proposed by Pinkel et al. (1991)

$$\frac{\partial \xi}{\partial z}(x, z_{\overline{\sigma}}) = \frac{N_b^2(z_{\overline{\sigma}})}{N^2[x, z(\overline{\sigma})]} - 1, \tag{4}$$

with $N_b^2(z_{\overline{\sigma}})$ the background stratification and $N^2[x, z(\overline{\sigma})]$ stratification at local depths.

Vertical strain ξ_z is also 2D-demeaned

$$\xi_z(x, z_{\overline{\sigma}}) = \xi_z'(x, z_{\overline{\sigma}}) + \overline{\xi_z}^{x}(z_{\overline{\sigma}}) + \overline{\xi_z}^{z_{\overline{\sigma}}}(x) + \overline{\xi_z}^{xz_{\overline{\sigma}}} \tag{5}$$

prior to computing its 2D wavenumber spectrum $\Phi[\xi_z'](k_x, k_z)$. This spectrum is identical to $(2\pi k_z)^2\Phi[\xi'](k_x, k_z)$.

5) ESTIMATES OF 1D AND 2D SPECTRUM OF ISOPYCNAL SALINITY GRADIENT

TCTD-measured salinity is projected onto isopycnals to examine the spectra of a passive tracer, for example, isopycnal spice $2\beta S'$ (where β is the saline-contraction coefficient). It is similarly decomposed into means and perturbation components

$$S(x, z_{\overline{\sigma}}) = S'(x, z_{\overline{\sigma}}) + \overline{S}^{x}(z_{\overline{\sigma}}) + \overline{S}^{z_{\overline{\sigma}}}(x) + \overline{S}^{xz_{\overline{\sigma}}}. \quad (6)$$

The 2D and 1D spectra of salinity gradient spectrum are computed in the same manner as isopycnal slope.

6) 2D SPECTRA CHARACTERISTICS

TCTD-inferred 2D wavenumber spectra are nearly symmetric across zero k_x and k_z [$\Phi(k_x, k_z) \approx \Phi(-k_x, k_z)$], suggesting horizontal isotropy and vertical symmetry, so only the $k_x, k_z > 0$ quadrant is presented for the TCTD3 2D wavenumber spectra for isopycnal slope (Fig. 7), vertical strain (Fig. 9), and isopycnal salinity gradient (Fig. 11). The 1D wavenumber spectra for isopycnal slope (Fig. 8), vertical strain (Fig. 10), and isopycnal salinity gradient (Fig. 12) were obtained by integrating over one dimension of the 2D spectra including negative wavenumbers.

2D wavenumber spectra for the TCTD3 sections span $2 \times 10^{-4} < k_x < 2 \times 10^{-2}$ cpm ($50 < \lambda_x < 5000$ m) and $2 \times 10^{-2} < k_z < 5 \times 10^{-1}$ cpm ($2 < \lambda_z < 48$ m). This corresponds to the submesoscale band in the horizontal and finescale band in the vertical, straddling the canonical internal wave vertical cutoff wavenumber $k_{z_c} \sim 0.1$ cpm (Gargett et al. 1981).

The 2D spectra allow examination of spectral properties in different wavenumber bands and different dynamic aspect ratios, e.g., with respect to Burger number $\mathrm{Bu} = (Nk_x/fk_z)^2$ (where $N \sim 9.5 \times 10^{-3}$ s^{-1} and $f \sim 8 \times 10^{-5}$ s^{-1}), which is expected to be >1 for 2D stratified turbulence and small-scale vortical motions (Müller 1984; Lindborg 2005; Kunze 2019). Previous observations of small-scale oceanic motions have Burger numbers of $\mathcal{O}(10^{-1}$–$10^{2})$ (Kunze 1993; Polzin et al. 2003; Pinkel 2014; Lien and Sanford 2019). TCTD3 2D wavenumber spectra (Figs. 7, 9, and 11) span aspect ratios k_x/k_z corresponding to $1.05f < \omega < N/2$ for linear internal waves for $k_z < 0.1$ cpm but only lower aspect ratios (internal waves frequencies) for $k_z > 0.1$ cpm. Observed spectra are compared to the Garrett–Munk (GM) internal wave spectral model (appendix C) for $k_z < 0.1$ cpm.

7) 2D SPECTRA INTERPOLATION AND NOISE CORRECTION

The 2D white-noise spectra associated with measurement uncertainty are computed from the average of 200 iterations for each section using artificial random noise. The ratio of spectra with and without interpolation correction was used as a transfer function to correct the observed 2D spectra, primarily for high-wavenumber attenuation due to interpolation onto a regular $(x, z_{\overline{\sigma}})$ grid. The interpolation correction also accounts for uncertainty in the projection due to ship ADCP spatial resolution. The EM-APEX float 1D k_z vertical strain spectrum (Fig. 10b) was similarly corrected for loss of variance due to interpolation using a transfer function from 1D white-noise spectral ratios.

The noise level for vertical isopycnal displacement was estimated as $\Delta\xi = \Delta\rho/\overline{\partial\rho/\partial z} = 0.45$ m, from instrument uncertainty $\Delta\rho = 3 \times 10^{-3}$ kg m^{-3} and median observed density gradient $\overline{\partial\rho/\partial z}$. The noise level for salinity was estimated as $\Delta S = 6.7 \times 10^{-3}$ psu from the RMS of the isopycnal projection uncertainty $\Delta z \times \partial S/\partial z = 0.5$ m $\times$ 0.012 psu m^{-1}, and sensor uncertainty 3×10^{-3} psu. The 2D noise spectra computed from regularly gridded random noise with normal distribution (with mean = 0 and standard deviation ΔS and $\Delta\xi$) were subtracted from the observed interpolation-corrected 2D spectra. Wavenumbers where $(\Phi_{\mathrm{TCTD}} - \Phi_{\mathrm{noise}})/\Phi_{\mathrm{TCTD}} < 0.2$ were discarded from analysis (Figs. 7, 9, and 11). This leads to underestimation of spectral levels and slopes near the Nyquist wavenumbers in 1D spectra (Figs. 8, 10, and 12). The effect of noise-level uncertainty on the corrected spectra was estimated by subtracting 2D noise spectra using nominal noise levels $\Delta\xi$ and $\Delta S \pm 20\%$.

3. Background conditions

The TCTD3 measurement site was chosen from the long TCTD1 and TCTD2 sections because of its strong compensated temperature and salinity variability in the 1-m resolution 69–117 m depth window (Figs. 3a–c and 4). TCTD depth profiles reveal a local subsurface salinity maximum at 100–120 m depth (Fig. 3b) associated with confluence of the surface southeastward California Current and the relatively warmer, more saline subsurface northwestward California Undercurrent. In a typical TCTD3 section, density fluctuations span a broad range of vertical and horizontal scales (Fig. 5a). There are strong salinity anomalies along both depth and density isolines (Fig. 5b).

Frequency spectra for horizontal kinetic energy (HKE) and available potential energy (APE) from EM-APEX float time series exhibit strong semidiurnal peaks (Fig. 6). HKE spectra also show a weak near-inertial peak. Spectral slopes in the internal wave continuum above tidal frequencies are consistent with the GM model (appendix C), with spectral levels a factor of 2 below canonical GM. Clockwise and counterclockwise energy ratios are consistent with linear internal wave theory (Fofonoff 1969; Lien and Müller 1992), suggesting energy is dominated by linear internal waves.

4. Isopycnal slope spectra

a. 2D spectrum

The mean 2D wavenumber spectrum for isopycnal slope $\Phi[\xi_x'](k_x, k_z)$ for all 136 TCTD3 sections (Fig. 7) increases with increasing k_x (blue spectrum) and decreasing k_z (red spectrum), i.e., increasing with increasing aspect ratios (k_x/k_z), such that there is negligible variance at the lowest resolved aspect ratios. Spectral values at the highest wavenumbers are influenced by noise. For $k_x > \sim 0.01$ cpm and $k_x > \sim 0.2$ cpm, where $(\Phi_{\mathrm{TCTD}} - \Phi_{\mathrm{noise}})/\Phi_{\mathrm{TCTD}} < 0.2$, spectra are considered dominated by noise and discarded from the analysis.

For $k_z < k_{z_c} \sim 0.1$ cpm, the 2D isopycnal slope spectrum resembles the GM internal wave model, suggesting that the observed isopycnal slope spectrum can be explained by internal

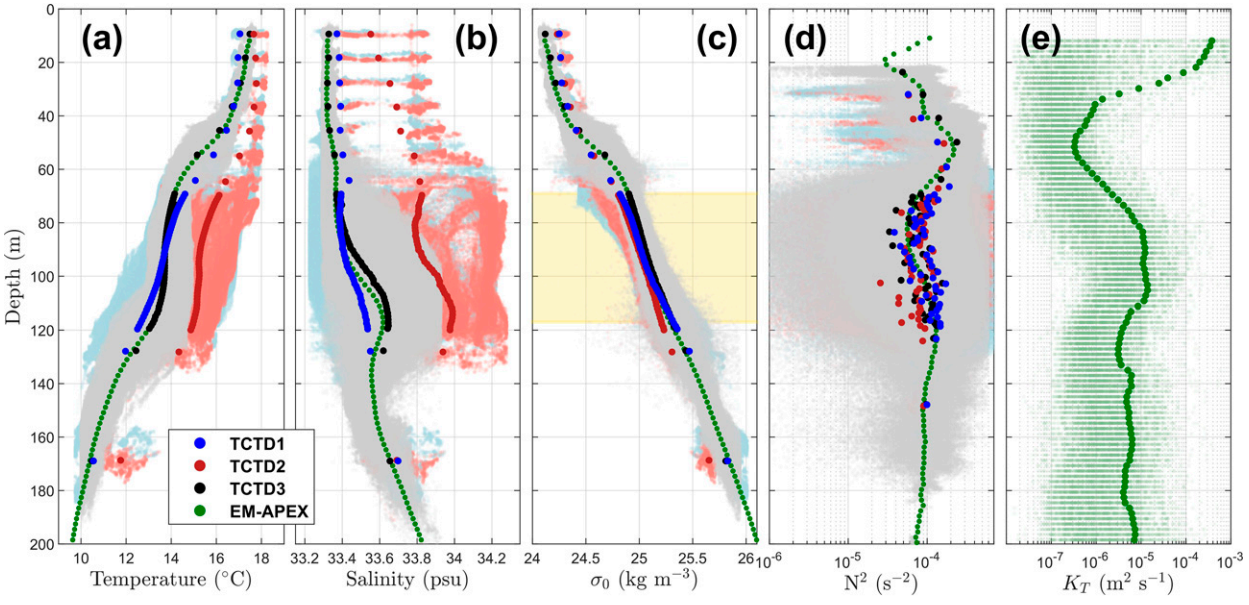

FIG. 3. Depth profiles of TCTD and mean EM-APEX float-measured (a) temperature T, (b) salinity S, (c) potential density σ_0, and (d) buoyancy stratification N^2, with instantaneous values lighter and averages darker. Yellow shading in (c) spans the depth window with ~1-m TCTD vertical resolution. (e) Depth profiles of EM-APEX float turbulent thermal diffusivity K_T during TCTD3 survey.

waves (Fig. 7). Spectral levels are a factor of 3 lower than GM, consistent with the float-measured internal wave field (Fig. 6). For $k_z > 0.1$ cpm, horizontal wavenumber spectra become progressively bluer (more positive slope) at higher k_z and vertical wavenumber spectra become less red (less negative slope) at higher k_x.

The 2D wavenumber spectra for isopycnal slope were integrated over different wavenumber bands to investigate 1D k_x and k_z spectral properties (Figs. 8a and 8b, respectively). The noise-dominated high wavenumbers of the spectrum are assumed equal to zero for the integrations.

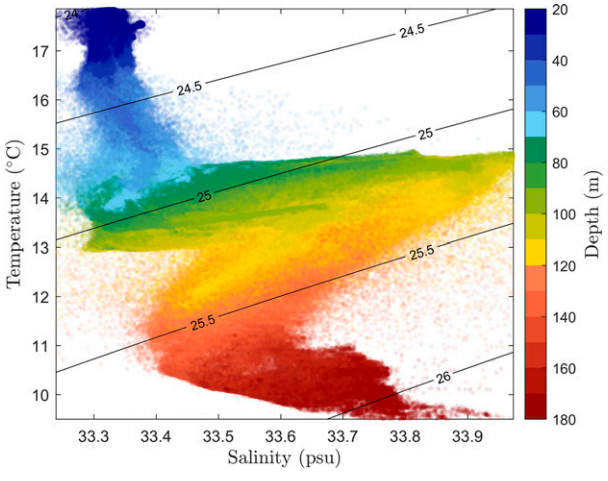

FIG. 4. Temperature-salinity diagram for the 136 TCTD3 sections with depth in color (green through yellow corresponding to the ~1-m vertical resolution TCTD depth window between 69- and 117-m depth). Black contours are potential density. There is a salinity maximum at ~110-m depth (σ_0 = 25.25 kg m^{-3}) and higher water-mass variability deeper than 70 m (denser than σ_0 = 24.75 kg m^{-3}).

b. 1D k_x spectra

The 1D horizontal wavenumber spectrum from vertical wavelengths $\lambda_z > 48$ m resembles GM but has lower spectral level for $k_x < \sim 10^{-3}$ cpm ($\lambda_x > 1$ km), where both internal wave and balanced contributions are expected (Fig. 8a). However, the GM spectrum has a broad spectral peak centered around $k_x = 2 \times 10^{-3}$ cpm, while the observed spectrum exhibits a plateau between $10^{-4} < k_x < 2 \times 10^{-3}$ cpm, rolling off at 2×10^{-3} cpm, and flattening again for $k_x > 4 \times 10^{-3}$ cpm.

The total spectrum, including all vertical scales > 2 m, has a roughly +1/3 slope for $k_x > \sim 3 \times 10^{-3}$ cpm, consistent with previous observations (Klymak and Moum 2007; Holbrook et al. 2013; Falder et al. 2016; Fortin et al. 2016), as well as anisotropic stratified turbulence numerical simulations (Riley and DeBruynkops 2003; Waite and Bartello 2004; Lindborg 2006; Brethouwer et al. 2007) and theoretical predictions (Kunze 2019). Integrated over resolved vertical wavenumbers ($2 < \lambda_z < 48$ m), the 1D k_x spectrum for isopycnal slope is blue with + 2/3 spectral slope (Fig. 8a). Further decomposition by vertical wavenumber band reveals that spectral levels are set by the $10 < \lambda_z < 48$ m internal wave subrange for $k_x < \sim 2 \times 10^{-3}$ cpm. The $2 < \lambda_z < 10$ m finescale subrange only contributes significant variance for $k_x > 5 \times 10^{-3}$ cpm ($\lambda_x < 200$ m). The k_x spectrum in the vertical finescale ($2 < \lambda_z < 10$ m) is blue with spectral slopes of +2 at low horizontal wavenumber, reflecting the lack of variance at low k_x and high k_z in the 2D spectrum (Fig. 7), transitioning to ~+1/2 for horizontal wavenumbers $k_x > \sim 3 \times 10^{-3}$ cpm. However, this spectral slope may be underestimated since the highest wavenumbers

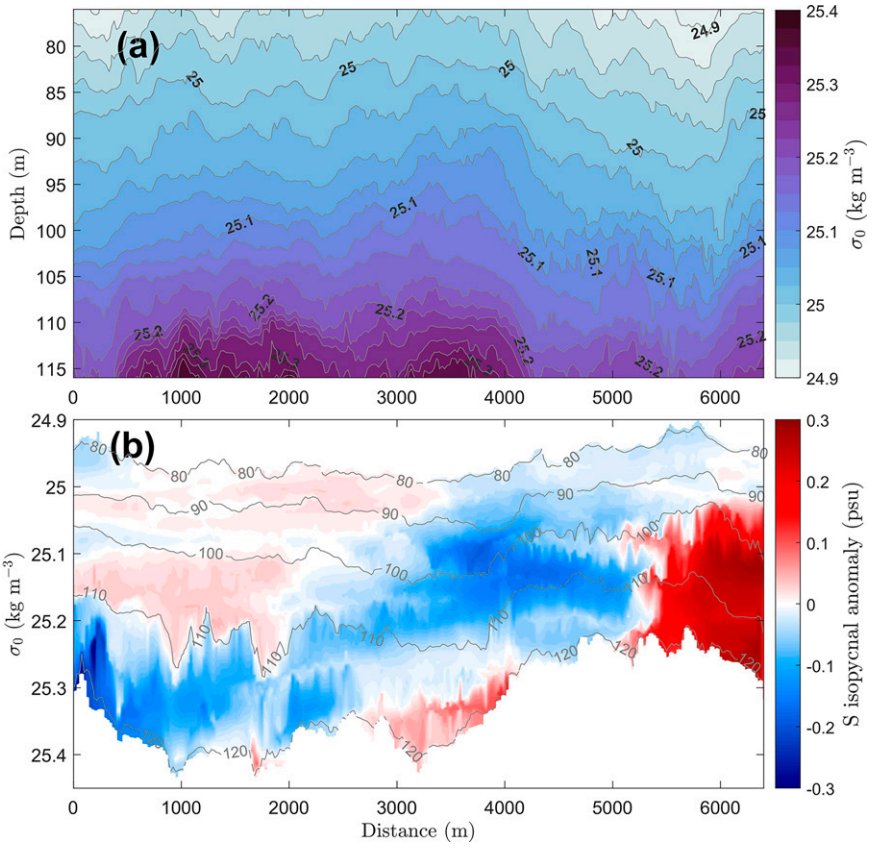

FIG. 5. Example TCTD3 section of (a) potential density $\sigma_0(x, z)$ from which isopycnal displacement ξ, and hence isopycnal slope ξ_x and vertical strain ξ_z are inferred; (b) salinity isopycnal anomaly (x, σ_0) with depth contours in gray, illustrating large salinity gradients along both density and depth.

have been discarded because of measurement noise. Nevertheless, it is a robust feature that the spectral slopes at high k_x become more positive for increasing vertical wavenumber bands.

Horizontal wavenumber spectral slopes in all vertical wavenumber bands, as well as their relative contribution, change above the horizontal Coriolis wavenumber $(f^3/\varepsilon)^{1/2}$ which has been argued to represent a transition (i.e., the lower-bound horizontal wavenumber) to anisotropic turbulence (Kunze 2019).

c. 1D k_z spectra

The 1D vertical wavenumber spectra of isopycnal slope are partitioned into different horizontal wavenumber bands (Fig. 8b). Integrated over all resolved horizontal wavenumbers ($\lambda_x > 50$ m), k_z spectra have slopes of ~ -1 at the lowest resolved vertical wavenumbers, rolling off with a -3 slope for $k_z > 0.15$ cpm $\sim(fN^2/\varepsilon)^{1/2}$. The spectral flattening above $k_z > 0.3$–0.4 cpm has large uncertainty and is likely due to imperfect correction for interpolation and noise. Vertical wavenumber spectra of isopycnal slope are dominated by the highest horizontal wavenumbers ($50 < \lambda_x < 200$ m), sensitive to interpolation and noise. In lower horizontal wavenumber bands, they are decades lower, reflecting that large horizontal fluctuations contribute little to isopycnal slope variance at small vertical scales (Fig. 7).

d. Summary

In summary, 2D wavenumber spectra for isopycnal slope are dominated by the highest measured horizontal wavenumbers, with spectral slopes ranging from 0 to +1 in k_x and 0 to −2 in k_z. They are consistent with the GM internal wave model for $\lambda_z > 48$ m at lower horizontal wavenumbers $k_x < 1 \times 10^{-3}$ cpm ($\lambda_x > 1$ km) (Figs. 7 and 8). High-k_x horizontal wavenumber spectra for all measured k_z ($\lambda_z > 2$ m) have roughly +1/3 spectral slopes (Fig. 8a), consistent with previous measurements and an anisotropic stratified turbulence theory (Kunze 2019). The +1/3 k_x spectral slope is contributed by $2 < \lambda_z < 48$ m, encompassing the vertical finescale subrange and the high-wavenumber end of weakly nonlinear internal waves. However, red vertical wavenumber spectra (Fig. 8b) are not consistent with k_z^{+3} theoretical predictions. Changes in spectral shapes above $\sim(f^3/\varepsilon)^{1/2}$ and $(fN^2/\varepsilon)^{1/2}$ suggest a shift to more nonlinear dynamics.

5. Vertical strain spectra

a. 2D spectrum

The mean 2D wavenumber spectrum for vertical strain $\Phi[\xi_z'](k_x, k_z)$ from the TCTD3 sections is dominated by low horizontal and vertical wavenumbers (Fig. 9). For $k_z < 0.1$ cpm, the spectral distribution in 2D wavenumbers resembles GM,

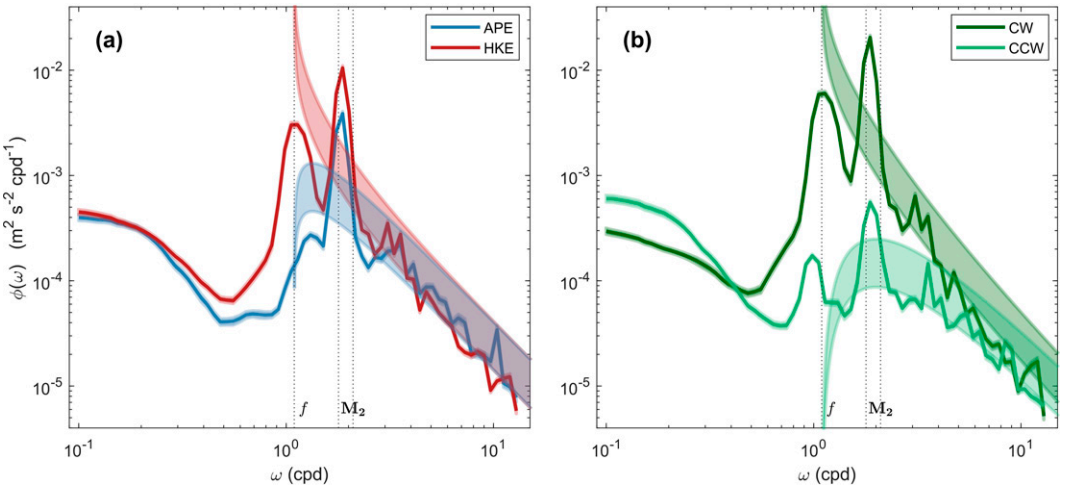

FIG. 6. Frequency spectra for (a) horizontal kinetic energy (HKE, blue) and available potential energy (APE, red), and (b) clockwise CW (dark green) and counterclockwise CCW (light green) velocity from the six EM-APEX profiling floats during TCTD3 (see Fig. 2b), averaged over 20–180-m depth. Light shading indicates GM spectra for the measured range of N. The M_2 semidiurnal frequency is bracketed by the floats' 1-h frequency resolution.

but with a weaker spectral level, consistent with the isopycnal slope spectrum (Fig. 7) and float frequency spectra (Fig. 6). For $k_z > 0.1$ cpm, k_x spectra become bluer and k_z spectra redder. The vertical strain spectrum is below the estimated noise level at the highest wavenumbers. The spectral peak shifts to higher k_x for $k_z > 0.1$ cpm, roughly following Bu = 1 with increasing k_x and k_z.

b. 1D k_z spectra

The 1D vertical wavenumber spectrum for vertical strain, integrated over all horizontal wavenumbers $k_x < 2 \times 10^{-2}$ cpm ($\lambda_x > 50$ m), is flat below $k_z \sim 0.15$ cpm and rolls off with a -1 slope at higher k_z, in agreement with previous measurements (Fig. 10b; Gregg 1977; Dewan 1979; Gargett et al. 1981; Fritts 1984; Fritts et al. 1988; Gregg et al. 1993). The flat spectrum for $k_z < 0.15$ cpm is a factor of ~2–3 lower than GM, consistent with Fig. 6 and the EM-APEX float vertical strain spectrum. Because of float CTD measurements' lower vertical resolution relative to the TCTD chain, a transfer function was applied to the float vertical strain spectrum to correct for lost variance at high k_z. The transfer function is derived as the ratio between the 1-m resolution TCTD spectrum and 2.6-m subsampled TCTD spectrum (equivalent to the average depth sampling interval of the floats). The corrected float spectrum reproduces the TCTD spectrum. The roll-off wavenumber of ~0.15 cpm is consistent with the prediction for saturated internal waves $k_{z_c} = (0.1 \text{ cpm})(E_{GM}/E) = (0.1 \text{ cpm})(\varepsilon_{GM}/\varepsilon)^{1/2}$ (Gargett et al. 1981; Henyey et al. 1986), where E_{GM} is the canonical GM spectral level and E the lower observed spectral level. It is also within the range of the measured vertical Coriolis wavenumber $(fN^2/\varepsilon)^{1/2} \sim 0.15$–$0.45$ cpm, which is the predicted lower vertical wavenumber bound for anisotropic turbulence (Kunze 2019), with scaling consistent with the finescale parameterization $\varepsilon \sim (E/E_{GM})^2$ (McComas and Müller 1981; Henyey et al. 1986).

For $k_z < 0.15$ cpm, most of the variance is contributed by $k_x < 1$ cpkm ($\lambda_x > 1$ km; Fig. 10b). Vertical wavenumber spectra from higher horizontal wavenumber bands are weaker and progressively bluer. Above the mean vertical Coriolis wavenumber $(fN^2/\varepsilon)^{1/2} \sim 0.3$ cpm, the shortest resolved horizontal wavelengths $50 < \lambda_x < 200$ are below the noise threshold so their spectrum rolls off excessively. Spectral levels and slopes are increasingly underestimated with increasing k_z and k_x. The -1 spectral slope characterizing the finescale ($k_z > 0.15$ cpm) is contributed by variance from increasing horizontal wavenumbers at increasing vertical wavenumbers, that is, from a roughly constant aspect ratio (Fig. 9).

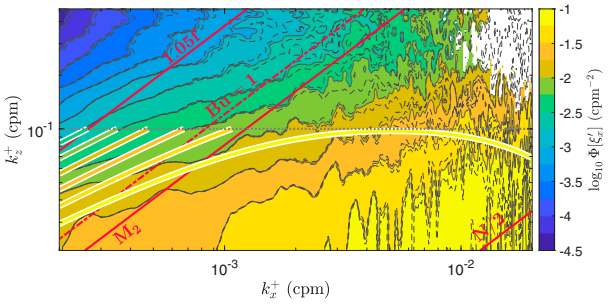

FIG. 7. Average 2D horizontal and vertical wavenumber spectrum for isopycnal slope $\Phi[\xi_x'](k_x, k_z)$ from 136 TCTD3 (x, z) sections (color and solid gray contours, 20% noise level uncertainty in dashed gray contours; high k_x and high k_z dominated by measurement noise in white and excluded from subsequent analysis). GM spectrum using mean measured N and f (white–color–white contours). Burger number Bu = $(Nk_x/fk_z)^2 = 1$ (dashed red line), and frequency isolines at $1.05f$, M_2 semidiurnal tide, and $N/2$ for linear internal waves (solid red lines).

c. 1D k_x spectra

Horizontal wavenumber spectra of vertical strain are red over the resolved k_x range (Fig. 10a). For larger vertical

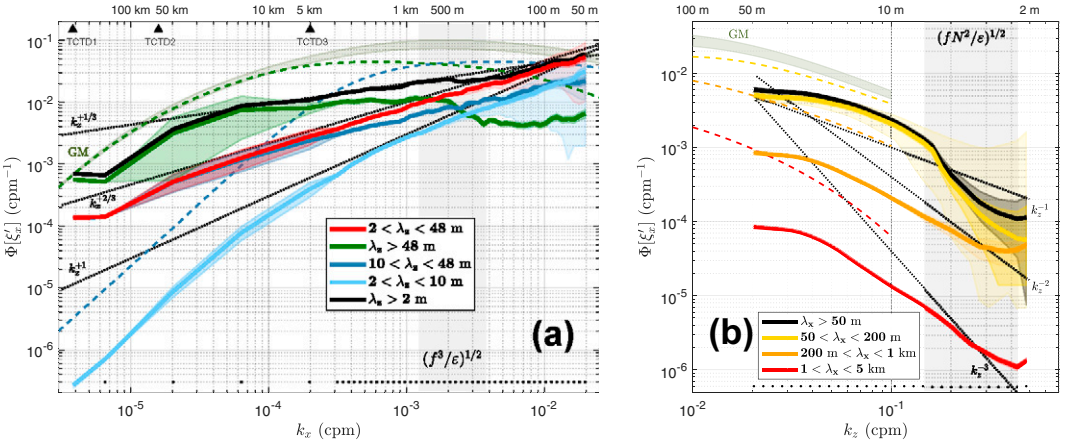

FIG. 8. (a) Average 1D horizontal wavenumber spectra for isopycnal slope $\Phi[\xi_x'](k_x)$ from TCTD1–3, in vertical wave bands: $2 < \lambda_z < 48$ m (red), $\lambda_z > 48$ m (green), $10 < \lambda_z < 48$ m (dark blue), $2 < \lambda_z < 10$ m (light blue), $\lambda_z > 2$ m (black), and (b) average 1D vertical wavenumber spectra for isopycnal slope: $50 < \lambda_x < 200$ m (yellow), $200 < \lambda_x < 1000$ m (orange), $1000 < \lambda_x < 5000$ m (red), and $\lambda_x > 50$ m (black). Dark shading indicates standard errors, light shading ±20% noise level uncertainty. Olive shading shows the spectral range of the GM model for $\lambda_z > 10$ m and $\lambda_x > 50$ m, for 90% of the observed N. Colored dashed lines show GM spectra in the corresponding wavenumber bands. Vertical gray shading shows 90% of the ranges of Coriolis wavenumbers $k_{x_f} = (f^3/\varepsilon)^{1/2}$ and $k_{z_f} = (fN^2/\varepsilon)^{1/2}$ based on float-measured ε. Black dotted diagonal lines indicate different spectral slopes for reference. Black triangles on upper x axis in (a) show maximum λ_x for TCTD1–3, and black dots on lower axes show the center of bins used in spectral averaging. The $2 < \lambda_z < 10$ m and $\lambda_z > 2$ m k_x spectra [light blue and black in (a)] are underestimated at high k_x because measurement noise precludes including the high-k_x and high-k_z parts of the 2D spectrum (Fig. 7). Likewise, the $\lambda_x > 50$ m and $50 < \lambda_x < 200$ m k_z spectra [black and yellow in (b)] are underestimated at high k_z because of omission of the noise-dominated part of the 2D spectrum (Fig. 7).

wavelengths $\lambda_z > 48$ m, spectral slopes lie between -1 and -2, resembling the GM spectral model. Except for the lowest k_x, the bulk of vertical strain variance is contributed by the vertical finescale ($2 < \lambda_z < 10$ m) which has -1 spectral slope, steepening at the highest wavenumbers where the spectra are underestimated because of discarded high-wavenumber variance (Fig. 9). A -1 spectral slope for $10^{-4} < k_x < 3 \times 10^{-3}$ cpm is consistent with anisotropic turbulence theory (Kunze 2019).

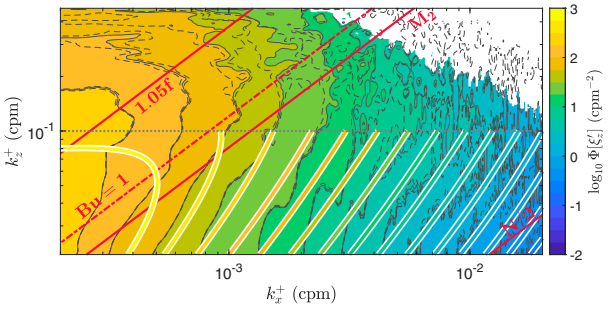

FIG. 9. Average 2D horizontal and vertical wavenumber spectrum for vertical strain $\Phi[\xi_z'](k_x, k_z)$ from 136 TCTD3 (x, z) sections (color and solid gray contours, 20% noise level uncertainty in dashed gray contours; high k_x and high k_z dominated by measurement noise in white and excluded from subsequent analysis). GM spectrum using mean measured N and f (white–color–white contours). Burger number $\mathrm{Bu} = (Nk_x/fk_z)^2 = 1$ dashed red line), and frequency isolines at 1.05f, M_2 semidiurnal tide, and $N/2$ for linear internal waves (solid red lines).

d. *Summary*

Spectra for vertical strain are largely consistent with the GM spectral model for $k_z < 0.15$ cpm and $k_x < 10^{-3}$ cpm, flat in vertical wavenumber with most variance contributed by low horizontal wavenumbers. For $k_z > 0.15$ cpm and $k_x > 10^{-3}$ cpm, both horizontal and vertical wavenumber spectra are red, with roughly -1 spectral slopes consistent with an anisotropic stratified turbulence model (Kunze 2019), though many other plausible explanations have been proposed.

6. Isopycnal salinity gradient spectra

a. *2D spectrum*

The average 2D wavenumber spectrum for isopycnal salinity gradient $\Phi[S_x'](k_x, k_z)$ from the 136 TCTD3 sections (Fig. 11) is dominated by low k_z and high k_x, resembling the 2D isopycnal slope spectrum (Fig. 7), especially for $k_z > 0.1$ cpm. Additionally, it exhibits a peak at the lowest k_x and k_z.

b. *1D k_x spectra*

Kunze et al. (2015) suggested that internal wave horizontal deformation might explain their observed isopycnal salinity gradient spectrum at horizontal scales of $\mathcal{O}(1)$ km. The k_x spectral shape for vertical wavelengths $\lambda_z > 48$ m (Fig. 12a) resembles the GM horizontal strain spectrum normalized by the observed large-scale salinity gradient for $k_x < \sim 10^{-3}$ cpm ($\lambda_x > 1$ km), but has a lower level. However, while the GM spectrum rolls off at higher k_x, the measured spectrum

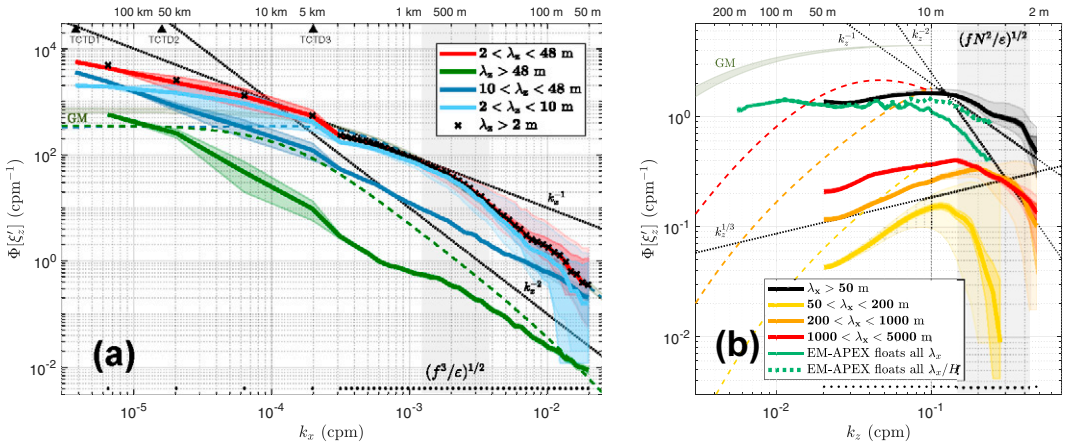

FIG. 10. (a) Average 1D horizontal wavenumber spectra for vertical strain $\Phi[\xi_z'](k_z)$ from TCTD1–3, in vertical wave bands: $2 < \lambda_z < 48$ m (red), $\lambda_z > 48$ m (green), $10 < \lambda_z < 48$ m (dark blue), $2 < \lambda_z < 10$ m (light blue), and $\lambda_z > 2$ m (black), and (b) 1D vertical wavenumber spectra for vertical strain in horizontal wave bands: $50 < \lambda_x < 200$ m (yellow), $200 < \lambda_x < 1000$ m (orange), $1000 < \lambda_x < 5000$ m (red), and $\lambda_x > 50$ m (black). The vertical wavenumber spectrum from EM-APEX floats in (b) (solid green) is corrected for lost variance at high k_z due to lower vertical resolution (dotted green), using transfer function H from the ratio between the 1-m resolution TCTD spectrum 2.6-m subsampled TCTD spectrum (equivalent to the average depth-sampling interval of the floats). Dark shading indicates standard errors, light shading ±20% noise-level uncertainty. Olive shading shows the spectral range of the GM model for $\lambda_z > 10$ m and $\lambda_x > 50$ m, for 90% of the observed N. Colored dashed lines show GM spectra in the corresponding horizontal wave bands. Vertical gray shading shows 90% of the ranges of Coriolis wavenumbers $k_{x_f} = (f^3/\varepsilon)^{1/2}$ and $k_{z_f} = (fN^2/\varepsilon)^{1/2}$ based on float-measured ε. Black dotted diagonal lines indicate different spectral slopes for reference. Black triangles on upper x axis in (a) show maximum λ_x for TCTD1–3, and black dots on lower axes show the center of bins used in spectral averaging. The $2 < \lambda_z < 10$ m and $\lambda_z > 2$ m k_x spectra [light blue and black in (a)] and $50 < \lambda_x < 200$ m k_z spectra [yellow in (b)] are underestimated at high k_x and high k_z, respectively, because measurement noise precludes including the high-k_x and high-k_z part of the 2D spectrum (Fig. 9).

remains flat, suggesting other processes take over the cascade of tracer variance. Comparing to Fig. 1c, the measured spectrum most resembles either GM plus anisotropic stratified turbulence or GM plus frontogenesis.

For $\lambda_z > 2$ m, the k_x spectrum has a roughly +1 slope for $k_x > 2 \times 10^{-3}$ cpm, consistent with nonlocal stirring and some previous observations (e.g., Klymak et al. 2015; Jaeger et al. 2020).

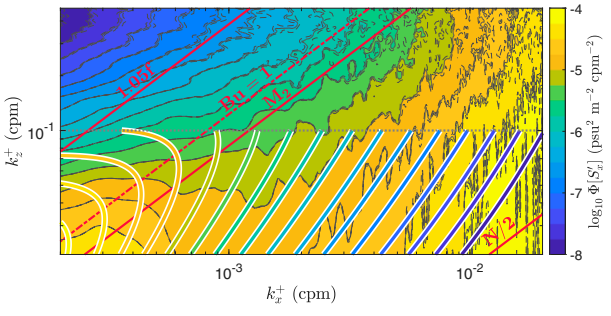

FIG. 11. Average 2D horizontal and vertical wavenumber spectrum for isopycnal salinity gradient $\Phi[S_x'](k_x, k_z)$ from 136 TCTD3 (x, z) sections (color and solid gray contours, 20% noise level uncertainty in dashed gray contours). GM spectrum using mean measured N and f (white–color–white contours). Burger number $\mathrm{Bu} = (Nk_x/fk_z)^2 = 1$ (dashed red line), and frequency isolines at $1.05f$, M_2 semidiurnal tide, and $N/2$ for linear internal waves (solid red lines).

The salinity gradient spectrum for resolved vertical wavelengths $2 < \lambda_z < 48$ m also has a slope of ~+1. At $k_x < 10^{-3}$ cpm, this is primarily contributed by vertical wavelengths larger than 10 m, i.e., the internal wave k_z subrange. For $k_x > (f^3/\varepsilon)^{1/2} \sim 2 \times 10^{-3}$ cpm, the finescale ($2 < \lambda_z < 10$ m) contribution to the salinity gradient spectrum dominates, with a +3/2 slope.

A horizontal shear peak near $k_x \sim \mathcal{O}(10^{-4})$ cpm, where the vertical finescale spectral slope changes, might produce a +1 spectral slope through nonlocal stirring (Batchelor 1959; Scott 2006). Double diffusion might also influence the salinity spectra on isopycnals in this subrange (Ruddick and Richards 2003). However, the measured spectral slopes may be biased by the choice in noise level close to Nyquist wavenumbers.

c. 1D k_z spectra

The vertical wavenumber spectrum for isopycnal salinity gradient (Fig. 12b) for $\lambda_x > 50$ m is dominated by the shortest wavelengths ($50 < \lambda_x < 200$ m) at all k_z. The spectrum for $\lambda_x > 50$ m is roughly flat for $k_z < 0.1$ cpm and rolls off slightly at $k_z > 0.1$ cpm, close to the vertical Coriolis wavenumber $(fN^2/\varepsilon)^{1/2}$. Spectra for longer horizontal wavelengths roll off more steeply. The spectrum for $\lambda_x > 50$ m above $k_z \sim 0.3$ cpm is relatively flat but unreliable because of uncertainty in the noise level.

d. Summary

The horizontal wavenumber spectrum for isopycnal salinity gradient has slopes of ~+1 above $k_x \sim 10^{-3}$ cpm. Previous

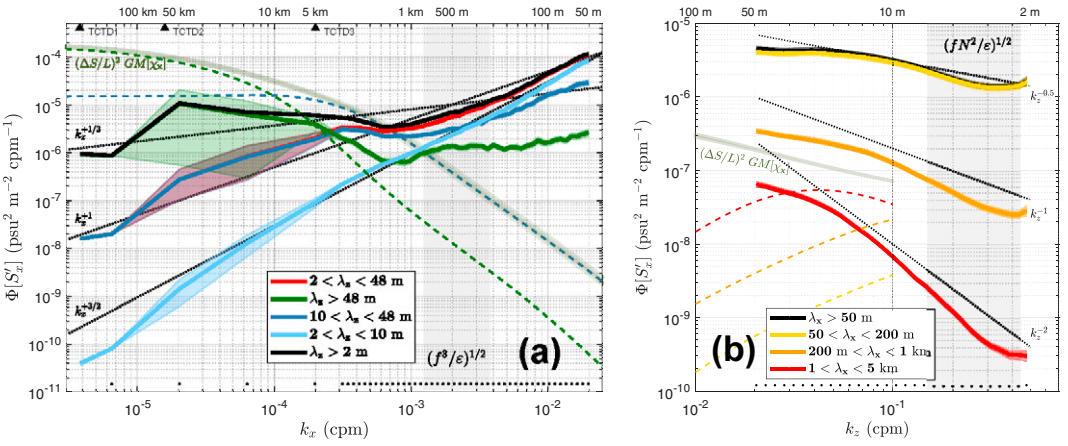

FIG. 12. (a) Average 1D horizontal wavenumber spectra for isopycnal salinity gradient $\Phi[S_x'](k_x)$ from TCTD1–3, in vertical wavelength bands: $2 < \lambda_z < 48$ m (red), $\lambda_z > 48$ m (green), $10 < \lambda_z < 48$ m (dark blue), $2 < \lambda_z < 10$ m (light blue), and $\lambda_z > 2$ m (black), and (b) 1D vertical wavenumber spectra for isopycnal salinity gradient in horizontal wave bands: $50 < \lambda_x < 200$ m (yellow), $200 < \lambda_x < 1000$ m (orange), $1000 < \lambda_x < 5000$ m (red), and $\lambda_x > 50$ m (black). Dark shading indicates standard errors, light shading ±20% noise level uncertainty. Olive shading shows the spectral range of the GM model for $\lambda_z > 10$ m and $\lambda_x > 50$ m, for 90% of the observed N. Colored dashed lines show GM spectra in the corresponding horizontal wave bands. Vertical gray shading shows 90% of the ranges of Coriolis wavenumbers $k_{x_f} = (f^3/\varepsilon)^{1/2}$ and $k_{z_f} = (fN^2/\varepsilon)^{1/2}$ based on float-measured ε. Black dotted diagonal lines indicate different spectral slopes for reference. Black triangles on upper x axis in (a) show maximum λ_x for TCTD1–3, and black dots on lower axes show the center of bins used in spectral averaging. The $2 < \lambda_z < 10$ m and $\lambda_z > 2$ m k_x spectra [light blue and black in (a)] and $50 < \lambda_x < 200$ m k_z spectra [yellow in (b)] may be biased at high k_x and high k_z, respectively, because of the choice of noise level.

observations have reported spectral slopes ranging from −1 to +1 at these horizontal scales (Cole and Rudnick 2012; Callies and Ferrari 2013; Klymak et al. 2015; Kunze et al. 2015; Jaeger et al. 2020). Kunze et al. (2015) argued that the spectra for the decade below $k_x \sim 10^{-3}$ cpm could be explained by GM internal wave horizontal deformation, which is consistent with this wavenumber subrange being dominated by vertical wavelengths exceeding 48 m (Fig. 12a). However, for $k_x \sim 10^{-3}$ cpm, the GM strain spectrum rolls off as k_x^{-2}, while the measured k_x spectrum is blue. All k_z contribute significantly for $k_x \sim 10^{-3}$ cpm. The k_x spectra for the resolved vertical wavenumbers ($2 < \lambda_z < 48$ m) have slopes between +1 and +3/2, which differ from both the shear +1/3 slope and strain −1 spectral slope predictions for anisotropic turbulence (Kunze 2019) but might be explained by nonlocal stirring (Batchelor 1959; Scott 2006). However, the vertical finescale contribution is likely biased low by the removal of noise.

7. Turbulence scaling and energy cascade

In this section, turbulent diapycnal diffusivity K scalings in the anisotropic turbulence ($2 < \lambda_z < 10$ m) band are compared with the well-established vertical-strain-based parameterization (Gregg and Kunze 1991; Polzin et al. 1995; Whalen et al. 2012; Kunze 2017) in the internal wave band ($\lambda_z > 10$ m) to test whether the finescale (anisotropic turbulence) subrange participates in the forward energy and passive tracer variance cascades to isotropic turbulence and dissipation.

Towed temperature measurements at fixed depths near the Hawaiian Ridge found +1/3 spectral slopes, with spectral levels that scaled with diapycnal diffusivity (Klymak and Moum 2007). Though their resolved wavenumbers extended decades below the Ozmidov wavenumber, they interpreted the +1/3 spectral slope as the inertial convective (IC) subrange of stratified turbulence (Batchelor 1959)

$$\Phi_{\xi_x}^{\mathrm{IC}}(k_x) = 4\pi \frac{\Gamma\varepsilon}{N_0^2}[C_T\varepsilon^{-1/3}(2\pi k_x)^{1/3}]\ (\mathrm{cpm}^{-1}), \qquad (7)$$

where $\Gamma = 0.2$ is the mixing coefficient (Gregg et al. 2018), N_0 the mean buoyancy frequency, and $C_T = 0.4$. This model has been widely used to estimate turbulent kinetic energy dissipation rate ε using horizontal wavenumber spectra of isopycnal slope inferred from seismic measurements (e.g., Sheen et al. 2009; Holbrook et al. 2013; Falder et al. 2016; Fortin et al. 2016; Tang et al. 2020, 2021).

Assuming turbulent diapycnal diffusivity $K = \Gamma\varepsilon N_0^{-2}$ (Osborn 1980), the inertial convective spectrum (7) can be expressed in terms of K as

$$\Phi_{\xi_x}^{\mathrm{IC}}(k_x) = 4\pi C_T \Gamma^{1/3} N_0^{-2/3} K^{2/3} (2\pi k_x)^{1/3}. \qquad (8)$$

Diffusivity $K[\Phi_{\xi_x}^{\mathrm{IC}}]$, estimated from an RMS fit of model spectrum (8) to the mean measured $\Phi[\xi_x'](k_x)$ for $k_x > 5 \times 10^{-3}$ cpm (Fig. 13), is (i) 6×10^{-5} m^2 s^{-1} for vertical wavelengths $\lambda_z > 2$ m, (ii) 4.9×10^{-5} m^2 s^{-1} for vertical wavelengths $2 < \lambda_z < 48$ m, and (iii) 1.7×10^{-5} m^2 s^{-1} for vertical wavelengths $2 < \lambda_z < 10$ m [estimates from maximum-likelihood fitting, e.g., Ruddick et al. (2000), are identical]. Estimates are larger than the average 1.2×10^{-5} m^2 s^{-1} diffusivity

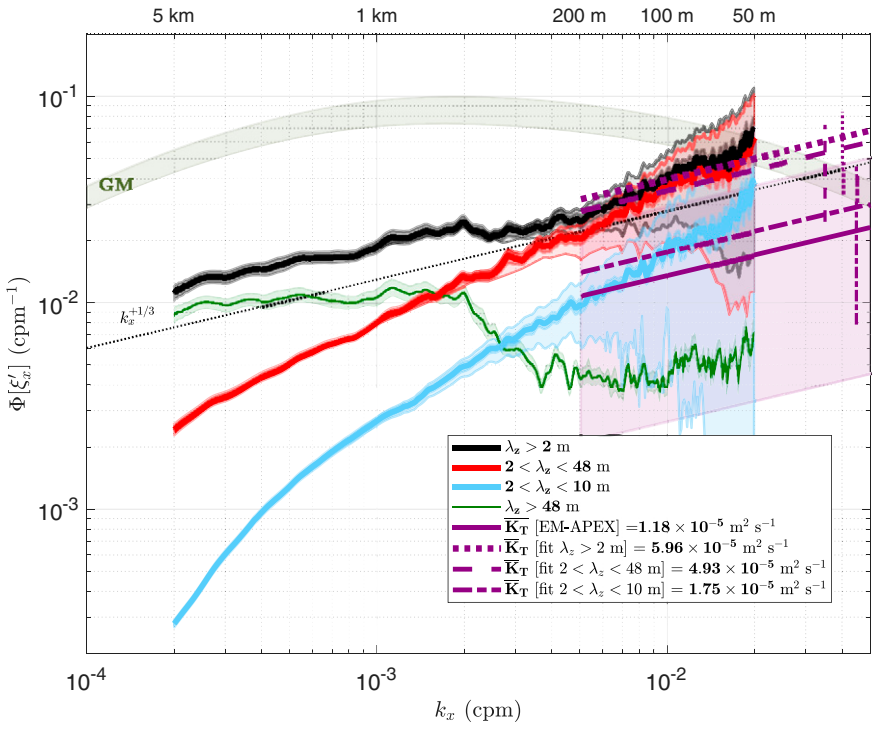

FIG. 13. Average horizontal wavenumber spectra of isopycnal slope $\Phi[\xi_x'](k_x)$ over 136 TCTD3 (x, z) sections integrated over all vertical wavelengths (black), resolved vertical wavelengths $2 < \lambda_z < 48$ m (red), small vertical wavelengths $2 < \lambda_z < 10$ m (light blue), and vertical wavelengths $\lambda_z > 48$ m (green), as well as GM spectrum for 90% of the observed N for $\lambda_z > 10$ m (olive shading). Dark shading indicates standard errors, light shading indicates ±20% noise level uncertainty. The purple solid line and shading represent the Batchelor (1959) and Klymak and Moum (2007) model spectra of inertial convective anisotropic turbulence $\Phi^{\mathrm{IC}}_{\xi_x}(k_x)$ [Eq. (8)] for $k_x > 5 \times 10^{-3}$ cpm using the mean (1.2×10^{-5} m^2 s^{-1}) and 90% of the float-measured K_T, respectively. The purple dotted, dashed, and dash–dotted lines represent linear least squares fits of observed $\Phi[\xi_x'](k_x)$ for $\lambda_z > 2$ m, $2 < \lambda_z < 48$ m, and $2 < \lambda_z < 10$ m, respectively, to the model spectrum $\Phi^{\mathrm{IC}}_{\xi_x}(k_x)$, corresponding to $K_T = 0.8 \times 10^{-4}$ m^2 s^{-1}, $K_T = 4.9 \times 10^{-5}$ m^2 s^{-1}, and $K_T = 1.7 \times 10^{-5}$ m^2 s^{-1}, respectively. Vertical purple lines indicate ±20% noise-level uncertainty. The dotted black diagonal line indicates a +1/3 spectral slope for reference.

inferred from the EM-APEX float χ measurements (Figs. 3e and 13), reflecting uncertainties in the correct wavenumber band to include and in $\mathcal{O}(1)$ nondimensional coefficients. This suggests a possible overestimation bias in the scaling induced by contributions from large vertical scales. This may impact published seismic estimates which include all vertical wavenumbers.

To examine interdependences, turbulent diapycnal diffusivity is estimated from the isopycnal slope variance $\langle \xi_x^2 \rangle$ integrated over $k_{x_{\min}} < k_x < k_{x_{\max}}$ and $0.02 < k_z < 0.5$ cpm ($2 < \lambda_z < 48$ m) for each TCTD3 section, following the spectral model in Eq. (8), as

$$K[\langle \xi_x^2 \rangle] = \frac{\langle \xi_x^2 \rangle^{3/2} N_0}{[3\pi(2\pi)^{1/3} C_T \Gamma^{1/2} (k_{x_{\max}}^{4/3} - k_{x_{\min}}^{4/3})]^{3/2}}. \qquad (9)$$

where $k_{x_{\min}} = 5 \times 10^{-3}$ cpm and $k_{x_{\max}} = 2 \times 10^{-2}$ cpm ($50 < \lambda_x < 200$ m). EM-APEX float microstructure measurements have 75% of their diapycnal diffusivities in the range 3×10^{-7} – 2×10^{-5} m^2 s^{-1} (Fig. 3e). Individual estimates of $K[\langle \xi_x^2 \rangle]$ from each section do not correlate well with simultaneous floats K_T estimates (not shown), likely because the 6 ± 4 km separations between concurrent TCTD3 and float profile measurements are longer than the expected turbulence patch horizontal length scale $\ell_x \sim \ell_z N/f \sim 0.1$–1 km for patch vertical length scales $\ell_z \sim 1$–10 m (Marmorino 1987; Marmorino et al. 1987; Itsweire et al. 1989; Rosenblum and Marmorino 1990; Marmorino and Trump 1991). This same issue prevents section-by-section comparisons between strain-based finescale parameterization estimates from the floats and TCTD chain.

Turbulent diapycnal diffusivity can also be inferred from TCTD-measured vertical strain variance $\langle \xi_z^2 \rangle$ in the internal wave band ($\lambda_z > 10$ m) using the finescale parameterization

$$K[\langle \xi_z^2 \rangle] = K_0 \frac{\langle \xi_z^2 \rangle^2}{\langle \xi_{z_{\mathrm{GM}}}^2 \rangle^2} g(R_\omega) h(f/N) \qquad (10)$$

(Polzin et al. 1995; Gregg et al. 2003; Kunze et al. 2006), where $\langle \xi_{z_{\mathrm{GM}}}^2 \rangle$ is GM vertical strain variance, $K_0 = 0.05 \times 10^{-4}$ m^2 s^{-1} the diapycnal diffusivity for the canonical GM internal wave field,

$$g(R_\omega) = \frac{1}{6\sqrt{2}} \frac{R_\omega(R_\omega + 1)}{\sqrt{R_\omega - 1}}, \quad (11)$$

$$R_\omega = \frac{\langle V_z^2 \rangle}{\overline{N}^2 \langle \xi_z^2 \rangle}, \quad (12)$$

$$h(f/N) = \frac{f \operatorname{arccosh}(N/f)}{f_{30} \operatorname{arccosh}(N_0/f_{30})}, \quad (13)$$

with $g(R_\omega) = 2.03$ for the mean float-measured shear-to-strain variance ratio $R_\omega = 5.6$ for $0.02 < k_z < 0.1$ cpm and 70–120-m depth, $f_{30} = f(30°)$, and $N_0 = 5.2 \times 10^{-3}$ rad s^{-1}. Internal wave strain variance is calculated from the TCTD3 2D vertical strain spectra (Fig. 9) integrated over $2 \times 10^{-4} < k_x < 10^{-3}$ cpm ($1 < \lambda_x < 5$ km) and $2 \times 10^{-2} < k_x < 0.1$ cpm ($10 < \lambda_z < 48$ m). GM strain variance $\langle \xi_{z_{GM}}^2 \rangle$ is calculated over the same k_x and k_z wavenumber bands.

These two independently inferred turbulent diapycnal diffusivities $K[\langle \xi_x^2 \rangle]$ and $K[\langle \xi_z^2 \rangle]$ are correlated (Fig. 14), with 49% of $K[\langle \xi_x^2 \rangle]$ within a factor of 5 of $K[\langle \xi_z^2 \rangle]$. This is larger than the factor of 2–3 scatter between microstructure measurements and the finescale parameterization in vertical profiles (Polzin et al. 1995; Whalen et al. 2012), but that is to be expected since the comparison is between two independent parameterizations. An orthogonal linear least squares fit in $\log_{10}$ space using $K[\langle \xi_x^2 \rangle]$ estimated from $2 < \lambda_z < 48$ m yields $\log_{10} K[\langle \xi_x^2 \rangle] = (1.19 \pm 0.31) \log_{10} K[\langle \xi_z^2 \rangle] + (1.6 \pm 1.42)$, with mean $K[\langle \xi_x^2 \rangle]/K[\langle \xi_z^2 \rangle] = 7.24 \pm 6.72$. Estimating $K[\langle \xi_x^2 \rangle]$ over a more restrictive $2 < \lambda_z < 10$ m yields $\log_{10} K[\langle \xi_x^2 \rangle] = (1.09 \pm 0.29) \log_{10} K[\langle \xi_z^2 \rangle] + (0.84 \pm 1.34)$, with mean $K[\langle \xi_x^2 \rangle]/K[\langle \xi_z^2 \rangle] = 2.58 \pm 3.38$ and 78% of $K[\langle \xi_x^2 \rangle]$ within a factor of 5 of $K[\langle \xi_z^2 \rangle]$. This correlation between $K[\langle \xi_z^2 \rangle]$ inferred from internal wave vertical strain and $K[\langle \xi_x^2 \rangle]$ inferred from the finescale subrange isopycnal slope variance is consistent with the hypothesis that the internal wave subrange ($\lambda_z > 10$ m) is connected to the isotropic turbulence subrange ($\lambda < 0.1$ m) by a forward energy cascade through the intermediate anisotropic stratified turbulence subrange (Kunze 2019).

In the presence of large-scale isopycnal water-mass gradients, turbulent mesoscale, submesoscale, and finescale flow fields will stir the gradients to cascade tracer variance to dissipative scales (e.g., Stern 1975; Ferrari and Polzin 2005). Isopycnal salinity gradient and isopycnal slope spectra exhibit similar horizontal and vertical spectral shapes (Figs. 8, 12). At horizontal wavelengths $50 < \lambda_x < 200$ m, salinity gradient and isopycnal slope variances are weakly correlated, with correlation coefficients $r = 0.64 \pm 0.02$ for $2 < \lambda_z < 48$ m and $r = 0.61 \pm 0.02$ for $2 < \lambda_z < 10$ m. The isopycnal salinity gradient spectrum is blue in the same k_x range interpreted as anisotropic stratified turbulence where the isopycnal slope spectrum has a +1/3 spectral slope. Thus, the correlation between variances of isopycnal slope and salinity gradient may imply a role for anisotropic turbulence in this wavenumber range in a forward salinity (passive tracer) variance cascade toward dissipation. Diffusivity $K[\langle S_x^2 \rangle]$ can be derived from scaled isopycnal salinity gradient spectra $\beta^2 \alpha^{-2} \Phi[S_x](k_x) \sim \Phi[T_x](k_x)$, where α and β are the thermal-expansion and saline-contraction coefficients, respectively, from

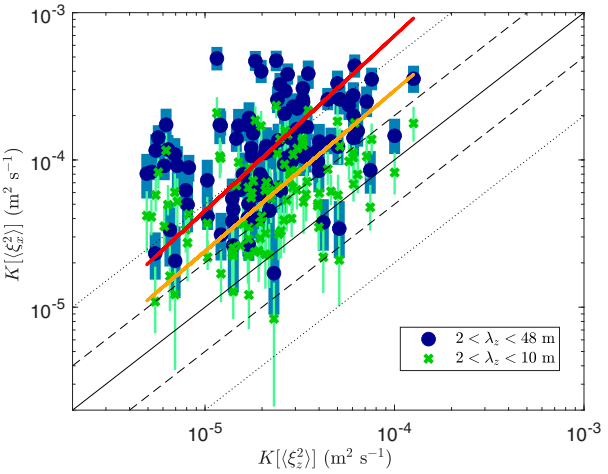

FIG. 14. Comparison of isopycnal-slope-inferred diapycnal diffusivities $K[\langle \xi_x^2 \rangle]$ and vertical-strain-inferred diffusivities $K[\langle \xi_z^2 \rangle]$ from TCTD3 measurements. $K[\langle \xi_x^2 \rangle]$ uses isopycnal slope variance $\langle \xi_x^2 \rangle$ from $50 < \lambda_x < 200$ m for the Batchelor (1959) parameterization [Eq. (9); Klymak and Moum 2007], for $2 < \lambda_z < 48$ m (dark blue) and $2 < \lambda_z < 10$ m (green). Circles and crosses show section-median values and vertical lines indicate 20% noise uncertainty. $K[\langle \xi_z^2 \rangle]$ uses vertical strain variance $\langle \xi_z^2 \rangle$ from $1 < \lambda_x < 5$ km and $10 < \lambda_z < 48$ m following the finescale parameterization [Eq. (10); Kunze et al. 2006]. Black diagonal lines show one-to-one dependence (solid), within factor of 2 (dashed) and within factor of 5 (dotted). The solid red line shows the orthogonal linear least squares fit in $\log_{10}$ space for $2 < \lambda_z < 48$ m, $\log_{10} K[\langle \xi_x^2 \rangle] = (1.19 \pm 0.31) \log_{10} K[\langle \xi_z^2 \rangle] + (1.6 \pm 1.42)$. The orange line is the fit for $2 < \lambda_z < 10$ m, $\log_{10} K[\langle \xi_x^2 \rangle] = (1.09 \pm 0.29) \log_{10} K[\langle \xi_z^2 \rangle] + (0.84 \pm 1.34)$.

Eq. (9) using the variance of the theoretical Batchelor (1959) spectrum

$$\Phi_{T_x}^{IC} = 4\pi C_T \Gamma^{1/3} N^{-2/3} \overline{T_z}^2 K^{2/3} (2\pi k_x)^{1/3}, \quad (14)$$

where $\overline{T_z}$ is the section-average vertical temperature gradient. The variance was calculated from TCTD3 1D k_x spectra (including all λ_z) over $5 \times 10^{-3} < k_x < 2 \times 10^{-2}$ cpm ($50 < \lambda_x < 200$ m). Section-mean $K[\langle S_x^2 \rangle]$ are correlated with $K[\langle \xi_x^2 \rangle]$ similarly inferred from the variance of the observed isopycnal slope 1D k_x spectrum over the same wavenumber band, with $\log_{10} K[\langle S_x^2 \rangle] = (1.15 \pm 0.11) \log_{10} K[\langle \xi_x^2 \rangle] + (1.24 \pm 0.41)$ (Fig. 15). This agreement holds for different horizontal wavenumber bands above $k_x > 10^{-3}$ ($\lambda_x < 1$ km). This suggests that the horizontal wavenumber subrange between internal waves and isotropic turbulence also participates in a turbulent scalar variance cascade.

8. Summary

The 2D wavenumber (k_x, k_z) spectra of upper-ocean isopycnal slope ξ_x, vertical strain ξ_z, and isopycnal salinity gradient S_x over 50 m $< \lambda_x <$ 250 km and $2 < \lambda_z < 48$ m, from towed CTD chain measurements, have been presented (Figs. 7, 9, and 11), affording a unique look of spectral properties in the underexplored horizontal mesoscale and submesoscale, and vertical finescale. Resolved vertical wavenumbers straddle the vertical strain $k_{z_c} \sim 0.1$ cpm roll-off (Gregg 1977; Gargett et al. 1981)

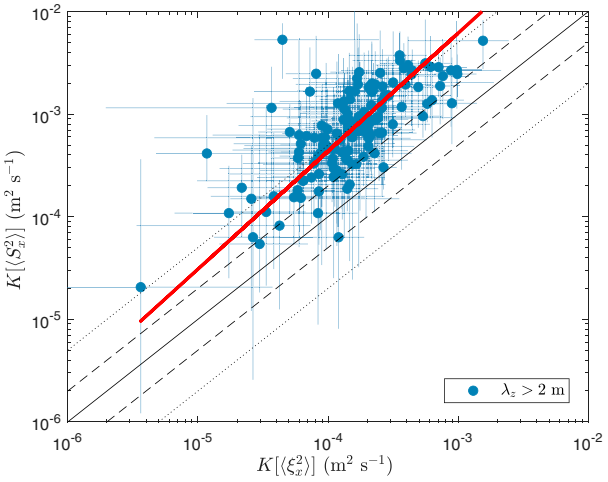

FIG. 15. Comparison of isopycnal-slope-inferred diapycnal diffusivities $K[\langle \xi_x^2 \rangle]$ and salinity gradient-inferred diffusivities $K[\langle S_x^2 \rangle]$ from TCTD3 measurements; $K[\langle S_x^2 \rangle]$ is inferred from the Batchelor (1959) parameterization [Eq. (9); Klymak and Moum 2007] using the variance of the scaled 1D isopycnal salinity gradient k_x spectrum $\beta^2\alpha^{-2}\Phi[S_x](k_x)$, for $50 < \lambda_x < 200$ m and $\lambda_z > 2$ m. $K[\langle \xi_x^2 \rangle]$ is inferred from Eq. (9) using the variance of the isopycnal slope 1D k_x spectrum, over the same k_x bands. Dots show section-median values and bars each section's 25th–75th percentiles. Black diagonal lines show one-to-one dependence (solid), within factor of 2 (dashed) and within factor of 5 (dotted). The solid red line shows the orthogonal linear least squares fit in $\log_{10}$ space, $\log_{10}K[\langle S_x^2 \rangle] = (1.15 \pm 0.11)\log_{10}K[\langle \xi_x^2 \rangle] + (1.24 \pm 0.41)$.

that marks the lower bound of the decade-wide subrange lying between weakly nonlinear internal waves ($k_z < 0.1$ cpm) and fully nonlinear isotropic turbulence (k_x, $k_z >$ 1–10 cpm) and which has been variously attributed to strongly nonlinear internal waves, kinematic distortion, vortical motions, thermohaline interleaving and anisotropic stratified turbulence.

Isopycnal slope k_x spectra exhibit a ~+1/3 spectral slope for $k_x > 3 \times 10^{-3}$ cpm (Fig. 8), consistent with previous observations (e.g., Klymak and Moum 2007; Sheen et al. 2009; Holbrook et al. 2013; Fortin et al. 2016; Falder et al. 2016), numerical modeling (e.g., Lindborg 2006; Brethouwer et al. 2007), and an anisotropic stratified turbulence spectral model (Kunze 2019). Salinity gradient k_x spectra have a +1 slope for $k_x > 2 \times 10^{-3}$ cpm (Fig. 12a), as reported in some previous studies (e.g., Klymak et al. 2015; Jaeger et al. 2020) and consistent with nonlocal stirring. The 1D vertical wavenumber spectra for vertical strain roll off at $k_z > 0.15$ cpm with a ~−1 spectral slope (Fig. 10b) as found in previous studies (e.g., Gregg 1977; Gargett et al. 1981; Gregg et al. 1993). The largest horizontal scales dominate below and near the roll-off vertical wavenumber k_{z_c}. Smaller horizontal scales contribute progressively more variance with increasing k_z.

For $k_z < 0.1$ cpm, observed 2D spectra are largely consistent with the GM internal wave model spectrum (Figs. 7–12), suggesting that internal waves dominate.

For isopycnal slope, isopycnal salinity gradient as well as vertical strain spectra, the smallest vertical (horizontal) scales contribute progressively more variance with increasing k_x (k_z), relative to larger λ_z (λ_x). This suggests a cascade of variance from lower to higher horizontal and vertical wavenumbers along a more constant aspect ratio or Bu trajectory, consistent with anisotropic turbulence theory. These results have significant uncertainties at high wavenumbers (~$k_x > 10^{-2}$ cpm, $k_z > 0.3$ cpm) where signals are noisy (e.g., Figs. 13, 10, and 12). Interpolation- and noise-corrected spectra presented here are likely redder than the true spectra close to Nyquist wavenumbers since some high-wavenumber variance is discarded to avoid noise contamination. The interpolation correction at the highest wavenumbers also is uncertain.

The measured spectra share many but not all properties of theoretical anisotropic stratified turbulence spectra (Kunze 2019). Anisotropic turbulence theory suggests that the horizontal $(\varepsilon/f^3)^{1/2}$ and vertical $(fN^2/\varepsilon)^{1/2}$ Coriolis wavenumbers are lower bounds of the anisotropic turbulence subrange (Kunze 2019). These roughly coincide with observed shifts in spectral shapes for isopycnal slope, isopycnal salinity gradient, and vertical strain 1D spectra (Figs. 8, 10, and 12). The roughly +1/3 spectral slope for $k_x > (\varepsilon/f^3)^{1/2} \sim 2 \times 10^{-3}$ cpm for isopycnal slope and −1 spectral slope for $k_z > (fN^2/\varepsilon)^{1/2} \sim$ 0.15 cpm for vertical strain are consistent with anisotropic turbulence predictions. Observed slopes for $k_x > (\varepsilon/f^3)^{1/2} \sim 2 \times 10^{-3}$ cpm for vertical strain are slightly redder than the predicted −1, but may be biased by noise removal. Theory predicts a +3 spectral slope in vertical wavenumber for isopycnal slope while negative slopes are observed (Fig. 8b). The +1 spectral slope for $k_x > (\varepsilon/f^3)^{1/2}$ cpm for isopycnal salinity gradient is consistent with nonlocal stirring but does not agree with the anisotropic turbulence model for horizontal shear (+1/3) or horizontal strain (−1). Thus, theoretical slope predictions are only partially consistent with measurements. These discrepancies may reflect inadequacies in anisotropic stratified turbulence theory, the presence of other dynamics, or measurement errors.

Independent inferences of turbulent diapycnal diffusivity K based on (i) vertical strain variance $\langle \xi_z^2 \rangle$ in the internal wave band ($10 < \lambda_z < 48$ m, $1 < \lambda_x < 5$ km) using a finescale parameterization (Gregg et al. 2003; Kunze et al. 2006), (ii) isopycnal slope variance $\langle \xi_x^2 \rangle$ in the anisotropic stratified turbulence band ($2 < \lambda_z < 48$ m, $50 < \lambda_x < 200$ m) (Batchelor 1959; Klymak and Moum 2007), and (iii) scaled isopycnal salinity gradient spectra variance in the anisotropic stratified turbulence band ($50 < \lambda_x < 200$ m, all λ_z) (Batchelor 1959; Klymak and Moum 2007) are correlated (Figs. 14, 15). This is consistent with the premise that the finescale band ($\lambda_z < 10$ m) participates in the forward energy and scalar variance cascades toward isotropic turbulence and dissipation.

Overall, these results support the hypotheses that internal waves can become anisotropically unstable at the finescale before vertical shear can overcome stratification, and that anisotropic turbulence at horizontal and vertical wavenumbers decades below the Ozmidov wavenumber bridges the forward energy and scalar variance cascades between internal waves and isotropic turbulence (Kunze 2019). Future and more accurate measurements spanning a wider range of turbulent intensity are needed to fully validate these conclusions.

9. Discussion

The horizontal and vertical wavenumber bands extending one decade in the vertical and several decades in the horizontal below the Ozmidov wavenumber $(N^3/\varepsilon)^{1/2}$ (the lowest wavenumber of isotropic turbulence) are spectrally distinct from the GM model spectrum at lower wavenumbers and isotropic turbulence at higher wavenumbers. Horizontal wavenumber spectra for isopycnal slope in this band exhibit a +1/3 spectral slope and scale with turbulent kinetic energy dissipation rate ε in the same manner as isotropic turbulence (Klymak and Moum 2007). Vertical wavenumber spectra for vertical strain in this band have a −1 spectral slope and are invariant with respect to changes in spectral levels both above the Ozmidov wavenumber and below the roll-off wavenumber ~0.1 cpm that is the upper bound of weakly nonlinear waves (Gargett et al. 1981). While finescale isopycnal salinity gradient spectral levels scale with those of finescale isopycnal slope, observed spectral slopes of +1 differ from anisotropic turbulence predictions, suggesting additional processes, such as nonlocal horizontal deformation or double diffusion, may be active in this subrange. Since previous observations found spectral slopes between −1 and +1 for $10^{-4} < k_x < 10^{-3}$ cpm (e.g., Klymak et al. 2015; Jaeger et al. 2020), the slopes reported in this study may be a smeared signature of superimposed intermittent processes at different stages of development.

While the 2D spectra of the horizontal submesoscale and vertical finescale wavenumber subranges presented here are consistent with past available 1D spectra and support some of the predictions of a theoretical anisotropic stratified turbulence spectrum (Kunze 2019), they have many limitations that require further investigation.

Nonnegligible uncertainty in the noise levels (e.g., Figs. 8, 12, and 10) may change the high-wavenumber spectral shapes significantly. Some noise in the signal is introduced by the projection of (x, y, z) measurements onto a regular (x, z) grid. The interpolation correction and noise subtraction have competing impacts on the highest wavenumbers. These limitations could be improved with higher-resolution measurements that would allow weaker isopycnal displacement and salinity gradient to be better resolved. Due to the finite size of the MicroCATs, cable sensor separation less than 1–1.5 m is not feasible. However, towing smaller temperature sensors in a region with a tight T–S relation could provide smaller uncertainties close to Nyquist wavenumbers.

Only water-mass measurements were made in the spectrally distinct subrange $k_x > (f^3/\varepsilon)^{1/2} \sim 10^{-3}$ cpm and $k_z > (fN^2/\varepsilon)^{1/2} \sim 0.15$ cpm. Measurements on similar scales of horizontal and vertical shear are needed to validate anisotropic turbulence dynamics, in particular, that vertical shears are $\mathcal{O}(N)$, and horizontal shears exceed f and increase to $\mathcal{O}(N)$ as k approaches the Ozmidov wavenumber.

The measurements spanned the predicted lower horizontal and vertical wavenumber bounds of anisotropic turbulence, $(f^3/\varepsilon)^{1/2}$ and $(fN^2/\varepsilon)^{1/2}$, but not those transitioning to isotropic turbulence at the Ozmidov wavenumber ~ $\mathcal{O}$(1–10) cpm.

Microstructure measurements from floats were not sufficiently collocated to test scaling with dissipation rate ε directly so that parameterizations were compared (Figs. 14, 15). Only a decade range of dissipation rate was sampled (Figs. 14, 15). Measurements are needed over a wider range of turbulent dissipation rates to test the dissipation rate scaling, with collocated microstructure measurements. Moreover, measurements allowing quantification of the spectral transfer rate (Lindborg and Cho 2000; Poje et al. 2017) are needed to determine if the cascade rate below the Ozmidov wavenumber matches the microscale dissipation rate ε.

While it is well established that most turbulence in the stratified ocean interior arises from shear instability of finescale low-frequency internal waves (Gregg et al. 1986; Hebert and Moum 1994; Peters et al. 1995; Polzin et al. 1995), how this instability can generate anisotropic stratified turbulence patches with $\mathcal{O}(f/N)$ aspect ratios is unknown since most numerical simulations have included neither horizontal background shear nor sufficiently low aspect ratios. Our present understanding of the wavenumber subranges extending up to several decades below the Ozmidov wavenumber, i.e., between weakly nonlinear internal gravity waves and isotropic turbulence, remains rudimentary. Sufficient measurements to provide guidance for rigorous theoretical advances are lacking, making this an area ripe for further research.

Acknowledgments. The authors thank Barry Ma, Avery Snyder, Ryan Newell, Jesse Dosher, and Tim McGinnes for instrument preparation and operation, Tom Sanford for the loan of EM-APEX floats, and the mates and crew of the R/V *Oceanus*. Undergraduate volunteers Rachel Mckenzie Scott and Ian Anderson Borchert, and graduate volunteers Zhihua Zheng, Erin Broatch, and Noah Shofer provided invaluable assistance in deploying and recovering the instruments. The authors also thank Jules Hummon of Shipboard ADCP Support Services at University of Hawaii for ADCP processing, two anonymous reviewers whose comments improved the manuscript, and Eric D'Asaro for inspiring discussions. This research was funded by NSF Grants OCE-1734160 and OCE-1734222.

Data availability statement. The data supporting the results presented in this study is available at https://digital.lib.washington.edu/researchworks/handle/1773/48343.

APPENDIX A

TCTD Space–Time Aliasing Verification

For internal waves, the horizontal and vertical wavenumber are connected to intrinsic frequency ω through the dispersion relation for linear internal waves

$$\omega^2 = \frac{N^2 k_h^2 + f^2 k_z^2}{k_h^2 + k_z^2}, \tag{A1}$$

where $k_h = (k_x^2 + k_y^2)^{1/2}$ is the horizontal wavenumber magnitude. The TCTD chain measurements were taken in one horizontal wavenumber direction and horizontal isotropy is assumed.

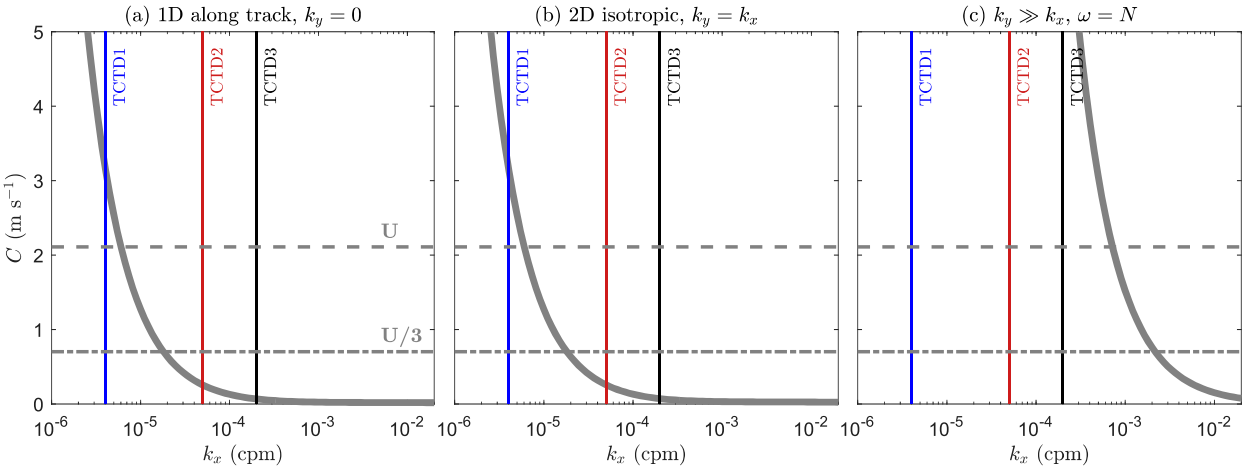

FIG. A1. Internal wave phase speed $C = \omega/k_x$ as a function of alongtrack wavenumber k_x (solid gray) for (a) across-track wavenumber $k_y = 0$ (anisotropic), (b) $k_y = k_x$ (isotropic), and (c) $k_y \gg k_x$ such that $\omega \sim N$ and $C \sim N/k_x$ (anisotropic). Dashed and dash–dotted gray horizontal lines denote mean sensor sampling speed U and $U/3$ inferred from the alongtrack water and ship speeds. Space–time aliasing will impact low alongtrack wavenumbers k_x where $C > U/3$ (to the left of the vertical lines), which are confined to the lowest measured wavenumbers of TCTD1 for the most plausible alongtrack and isotropic scenarios in (a) and (b), respectively.

Space–time aliasing is an issue for alongtrack internal wave phase speeds $C = C_x > U$, where $U \sim 2$ m s^{-1} is the tow speed. From dispersion relation (A1), the alongtrack internal wave phase speed is

$$C = C_x = \frac{[f^2k_z^2 + N^2(k_x^2 + k_y^2)]^{1/2}}{k_x(k_z^2 + k_x^2 + k_y^2)^{1/2}}, \qquad \text{(A2)}$$

where k_x and k_y are the along- and across-track wavenumbers with k_y unknown. Figure A1 shows the k_x ranges where (i) $C < U/3$ with negligible space–time aliasing, (ii) $U/3 < C < U$ where space–time aliasing may be an issue, and (iii) $C > U$ where space–time aliasing dominates. Three cases are considered: an anisotropic internal wave field with $k_y = 0$ (Fig. A1a), an isotropic field with $k_y = k_x$ (Fig. A1b), and an anisotropic field with $k_y \gg k_x$ such that $\omega \sim N$ and $C \sim N/k_x$ (Fig. A1c). There is little difference between the first two more plausible scenarios, which suggests that only the lowest $k_x < \sim 10^{-5}$ cpm of TCTD1 might be impacted by space–time aliasing. Thus, the high horizontal wavenumbers of primary interest in this study should be free of space–time aliasing.

APPENDIX B

TCTD Measurements Projection onto 2D Horizontal–Vertical Grid

The TCTD chain surveys are augmented with ocean current measurements of 8-m vertical and 250-m horizontal resolution from a shipboard 75-kHz acoustic Doppler current profiler (ADCP) used to infer the alongtrack water velocity. The TCTD time series, collected as a function of time and pressure every $\delta t = 12$ s, were projected onto an alongtrack horizontal–vertical grid. For each MicroCAT, the alongtrack horizontal displacement is a combination of (i) displacement due to movement of the ship and water relative to Earth $\delta x_u(z, t) = [u_{\text{ship}}(t) - u_{\|}(z, t)]\delta t \sim 23.5$ m, where ship speed $u_{\text{ship}} \sim 2$ m s^{-1} and alongtrack water speed $u_{\|} \sim 0.1$ m s^{-1}, and (ii) chain displacement behind the ship $\Delta x(z, t) \sim -(50\text{–}250)$ m (Fig. B1), which are computed separately for each section. The horizontal displacement of individual sensors relative to the shipboard ADCP system point of reference Δx is trigonometrically inferred from measured pressure and placement of sensors on the cable. Because of varying ship speed and cable drag, the chain changes its shape so that Δx is not invariant with time and depth. The position of each sensor on the horizontal grid is then $x(z, t) = \int(u_{\text{ship}} - u_{\|})dt - \Delta x$.

The data, as a function of $x(t)$ and $z(t)$, are then interpolated onto a regular 2D grid with $\delta x \sim 25$ m (median of the lowest 10% of δx_u) and $\delta z = 1$ m for computing 2D wavenumber spectra. Alongtrack water displacements due to water flow relative to Earth $u_{\|}\delta t$ were included for completeness but their inclusion has no significant impact on the spectra. Neglected across-track water displacements are likewise assumed not to have significant impact on the spectra.

APPENDIX C

Garrett–Munk Internal-Wave Spectral Model

The Garrett–Munk (GM) internal wave spectral model was empirically developed to describe the distribution of ocean internal wave energy in frequency–wavenumber space (Garrett and Munk 1972, 1975). The GM frequency spectra for horizontal kinetic energy $\Phi_{\text{GM}}[\text{HKE}]$, available potential energy $\Phi_{\text{GM}}[\text{APE}]$ are

$$\Phi_{\text{GM}}[\text{HKE}](\omega) = \frac{1}{\pi} b^2 N N_0 E_0 \frac{f(N^2 - \omega^2)(\omega^2 + f^2)}{\omega^3 N^2(\omega^2 - f^2)^{1/2}}, \qquad \text{(C1)}$$

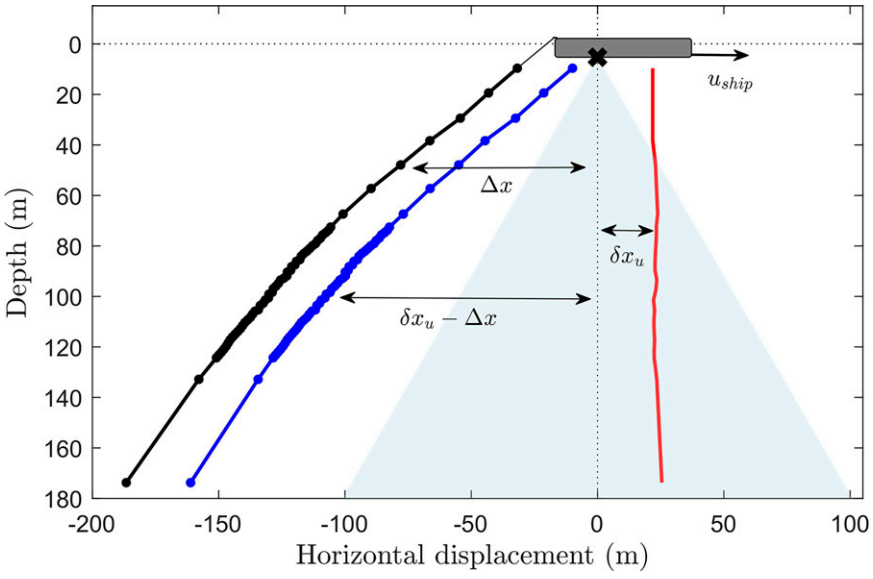

FIG. B1. Schematic illustrating individual CTD sensors instantaneous horizontal displacement $\delta xu - \Delta x$ (blue) at $t = \delta t$, constructed from (i) movement of the ship and water relative to Earth $\delta x_u = (u_{\text{ship}} - u_{\|})\delta t$ (red) where u_{ship} is ship speed, $u_{\|}$ ADCP-measured alongtrack water speed, and δt the sampling period, and (ii) chain displacement behind the ship Δx (black). Circles on towed chain represent CTD sensors, black cross shipboard ADCP, and light blue triangle ADCP cone illustrating that the CTD chain and ADCP measurements were not collocated.

$$\Phi_{\text{GM}}[\text{APE}](\omega) = \frac{1}{\pi} b^2 N N_0 E_0 \frac{f(\omega^2 - f^2)^{1/2}}{\omega^3}, \tag{C2}$$

and rotary clockwise $\Phi_{\text{GM}}[\text{CW}]$ and counterclockwise $\Phi_{\text{GM}}[\text{CCW}]$

$$\Phi_{\text{GM}}[\text{CW}](\omega) = \frac{1}{\pi} b^2 N N_0 E_0 \frac{f(N^2 - \omega^2)(\omega + f)^2}{\omega^3 N^2(\omega^2 - f^2)^{1/2}}, \tag{C3}$$

$$\Phi_{\text{GM}}[\text{CCW}](\omega) = \frac{1}{\pi} b^2 N N_0 E_0 \frac{f(N^2 - \omega^2)(\omega - f)^2}{\omega^3 N^2(\omega^2 - f^2)^{1/2}}, \tag{C4}$$

where pycnocline length scale $b = 1300$ m, $N_0 = 5.2 \times 10^{-3}$ s^{-1}, and nondimensional spectral level $E_0 = 6 \times 10^{-5}$.

The GM frequency and vertical wavenumber spectrum for total internal wave energy is

$$\Phi_{\text{GM}}[E](\omega, k_z) = \frac{2}{\pi} b^2 N N_0 E_0 \frac{f}{\omega} \frac{1}{\sqrt{\omega^2 - f^2}} \frac{k_z^\star}{(k_z^\star + k_z)^2}, \tag{C5}$$

where peak vertical wavenumber $k_z^\star = j^\star(\pi/b)(N/N_0)$ and peak mode number $j^\star = 3$. The GM vertical isopycnal displacement spectrum is

$$\begin{aligned}\Phi_{\text{GM}}[\xi](\omega, k_z) &= \frac{\omega^2 - f^2}{\omega^2 N^2} \Phi_{\text{GM}}[E](\omega, k_z) \\ &= 2bE_0 j^\star f \frac{(\omega^2 - f^2)^{1/2}}{\omega^3 (k_z^\star + k_z)^2}.\end{aligned} \tag{C6}$$

It can be expressed as a function of horizontal and vertical wavenumbers using the dispersion relation (A1):

$$\Phi_{\text{GM}}[\xi](k_x, k_y, k_z) = \frac{1}{\pi} bE_0 j^\star f \times \frac{k_h k_z^2 (N^2 - f^2)^{3/2}}{(k_h^2 N^2 + k_z^2 f^2)^2 (k_h^2 + k_z^2)^{1/2} (k_z^\star + k_z)^2}. \tag{C7}$$

A vertical wavenumber cutoff at 0.1 cpm was applied to $\Phi_{\text{GM}}[\xi](\omega, k_z)$ with the assumption that higher k_z are not weakly nonlinear internal waves. The $\Phi_{\text{GM}}[\xi](k_z, k_x)$ was obtained by numerically integrating the nonseparable $\Phi_{\text{GM}}[\xi](k_x, k_y, k_z)$ over k_y at each k_x and k_z. The 2D horizontal–vertical wavenumber spectrum of isopycnal slope is $\Phi_{\text{GM}}[\xi_x](k_x, k_z) = k_x^2 \Phi_{\text{GM}}[\xi](k_x, k_z)$ and the vertical strain spectrum is $\Phi_{\text{GM}}[\xi_z](k_x, k_z) = k_z^2 \Phi_{\text{GM}}[\xi](k_x, k_z)$. This is equivalent to Eqs. (3) and (4).

The GM horizontal strain in terms of frequency ω and vertical wavenumber k_z is

$$\Phi_{\text{GM}}[\chi_x](\omega, k_z) = \pi b E_0 j^\star \frac{(\omega^2 + f^2)(\omega^2 - f^2)^{1/2}}{\omega^5} \frac{k_z^2}{(k_z^\star + k_z)^2} \tag{C8}$$

(Kunze et al. 2015), which can be expressed in terms of wavenumbers k_x, k_y, and k_z as

$$\begin{aligned}\Phi_{\text{GM}}[\chi_x](k_x, k_y, k_z) = \frac{1}{\pi} bE_0 j^\star f (N^2 - f^2) \\ \times \frac{(2f^2 k_z + f^2 k_h^2 + N^2 k_h^2)(N^2 k_h^2 - f^2 k_h^2)^{1/2}}{(k_z^2 + k_h^2)^{1/2} (N^2 k_h^2 + f^2 k_z^2)^3} \\ \times \frac{k_z^4}{(k_z + k_z^\star)^2},\end{aligned} \tag{C9}$$

where the nonseparable (k_x, k_z) spectrum was computed by numerically integrating over k_y for each k_x and k_z.

REFERENCES

Batchelor, G. K., 1959: Small-scale variation of convected quantities like temperature in turbulent fluid. Part 1. General discussion and the case of small conductivity. *J. Fluid Mech.*, **5**, 113–133, https://doi.org/10.1017/S002211205900009X.

Billant, P., and J.-M. Chomaz, 2000: Experimental evidence for a new instability of a vertical columnar vortex pair in a strongly stratified fluid. *J. Fluid Mech.*, **418**, 167–188, https://doi.org/10.1017/S0022112000001154.

——, and ——, 2001: Self-similarity of strongly stratified inviscid flows. *Phys. Fluids*, **13**, 1645–1651, https://doi.org/10.1063/1.1369125.

Brethouwer, G., P. Billant, E. Lindborg, and J.-M. Chomaz, 2007: Scaling analysis and simulation of strongly stratified turbulent flows. *J. Fluid Mech.*, **585**, 343–368, https://doi.org/10.1017/S0022112007006854.

Callies, J., and R. Ferrari, 2013: Interpreting energy and tracer spectra of upper-ocean turbulence in the submesoscale range (1–200 km). *J. Phys. Oceanogr.*, **43**, 2456–2474, https://doi.org/10.1175/JPO-D-13-063.1.

Capet, X., J. C. McWilliams, M. J. Molemaker, and A. F. Shchepetkin, 2008a: Mesoscale to submesoscale transition in the California Current System. Part I: Flow structure, eddy flux, and observational tests. *J. Phys. Oceanogr.*, **38**, 29–43, https://doi.org/10.1175/2007JPO3671.1.

——, ——, ——, and ——, 2008b: Mesoscale to submesoscale transition in the California Current System. Part III: Energy balance and flux. *J. Phys. Oceanogr.*, **38**, 2256–2269, https://doi.org/10.1175/2008JPO3810.1.

Chereskin, T., M. Morris, P. Niiler, P. M. Kosro, R. L. Smith, S. Ramp, C. Collins, and D. Musgrave, 2000: Spatial and temporal characteristics of the mesoscale circulation of the California Current from eddy-resolving moored and shipboard measurements. *J. Geophys. Res.*, **105**, 1245–1269, https://doi.org/10.1029/1999JC900252.

Cole, S. T., and D. L. Rudnick, 2012: The spatial distribution and annual cycle of upper ocean thermohaline structure. *J. Geophys. Res.*, **117**, C02027, https://doi.org/10.1029/2011JC007033

Dewan, E., 1979: Stratospheric wave spectra resembling turbulence. *Science*, **204**, 832–835, https://doi.org/10.1126/science.204.4395.832.

——, 1997: Saturated-cascade similitude theory of gravity wave spectra. *J. Geophys. Res.*, **102**, 29 799–29 817, https://doi.org/10.1029/97JD02151.

——, and R. Good, 1986: Saturation and the "universal" spectrum for vertical profiles of horizontal scalar winds in the atmosphere. *J. Geophys. Res.*, **91**, 2742–2748, https://doi.org/10.1029/JD091iD02p02742.

Douglas, W., and R. Lueck, 2015: ODAS MATLAB Library technical manual, version 4.0. Rockland Scientific International Inc., https://rocklandscientific.com/support/despiking-data/.

Falder, M., N. J. White, and C.-P. Caulfield, 2016: Seismic imaging of rapid onset of stratified turbulence in the South Atlantic Ocean. *J. Phys. Oceanogr.*, **46**, 1023–1044, https://doi.org/10.1175/JPO-D-15-0140.1.

Ferrari, R., and K. L. Polzin, 2005: Finescale structure of the *T*–*S* relation in the eastern North Atlantic. *J. Phys. Oceanogr.*, **35**, 1437–1454, https://doi.org/10.1175/JPO2763.1.

Flament, P., L. Armi, and L. Washburn, 1985: The evolving structure of an upwelling filament. *J. Geophys. Res.*, **90**, 11 765–11 778, https://doi.org/10.1029/JC090iC06p11765.

Fofonoff, N., 1969: Spectral characteristics of internal waves in the ocean. *Deep-Sea Res. Oceanogr. Abstr.*, **16** (Suppl.), 59–71.

Fortin, W. F., W. S. Holbrook, and R. W. Schmitt, 2016: Mapping turbulent diffusivity associated with oceanic internal lee waves offshore Costa Rica. *Ocean Sci.*, **12**, 601–612, https://doi.org/10.5194/os-12-601-2016.

Fritts, D. C., 1984: Gravity wave saturation in the middle atmosphere: A review of theory and observations. *Rev. Geophys.*, **22**, 275–308, https://doi.org/10.1029/RG022i003p00275.

——, T. Tsuda, S. Kato, T. Sato, and S. Fukao, 1988: Observational evidence of a saturated gravity wave spectrum in the troposphere and lower stratosphere. *J. Atmos. Sci.*, **45**, 1741–1759, https://doi.org/10.1175/1520-0469(1988)045<1741:OEOASG>2.0.CO;2.

Galperin, B., S. Sukoriansky, and B. Qiu, 2021: Seasonal oceanic variability on meso-and submesoscales: A turbulence perspective. *Ocean Dyn.*, **71**, 475–489, https://doi.org/10.1007/s10236-021-01444-1.

Gargett, A., P. Hendricks, T. Sanford, T. Osborn, and A. Williams, 1981: A composite spectrum of vertical shear in the upper ocean. *J. Phys. Oceanogr.*, **11**, 1258–1271, https://doi.org/10.1175/1520-0485(1981)011<1258:ACSOVS>2.0.CO;2.

Garrett, C., and W. Munk, 1972: Space–time scales of internal waves. *Geophys. Fluid Dyn.*, **3**, 225–264, https://doi.org/10.1080/03091927208236082.

——, and ——, 1975: Space–time scales of internal waves: A progress report. *J. Geophys. Res.*, **80**, 291–297, https://doi.org/10.1029/JC080i003p00291.

——, and ——, 1979: Internal waves in the ocean. *Annu. Rev. Fluid Mech.*, **11**, 339–369, https://doi.org/10.1146/annurev.fl.11.010179.002011.

Gregg, M. C., 1977: Variations in the intensity of small-scale mixing in the main thermocline. *J. Phys. Oceanogr.*, **7**, 436–454, https://doi.org/10.1175/1520-0485(1977)007<0436:VITIOS>2.0.CO;2.

——, and E. Kunze, 1991: Shear and strain in Santa Monica basin. *J. Geophys. Res.*, **96**, 16 709–16 719, https://doi.org/10.1029/91JC01385.

——, E. D'Asaro, T. Shay, and N. Larson, 1986: Observations of persistent mixing and near-inertial internal waves. *J. Phys. Oceanogr.*, **16**, 856–885, https://doi.org/10.1175/1520-0485(1986)016<0856:OOPMAN>2.0.CO;2.

——, D. Winkel, and T. Sanford, 1993: Varieties of fully resolved spectra of vertical shear. *J. Phys. Oceanogr.*, **23**, 124–141, https://doi.org/10.1175/1520-0485(1993)023<0124:VOFRSO>2.0.CO;2.

——, T. B. Sanford, and D. P. Winkel, 2003: Reduced mixing from the breaking of internal waves in equatorial waters. *Nature*, **422**, 513–515, https://doi.org/10.1038/nature01507.

——, E. D'Asaro, J. Riley, and E. Kunze, 2018: Mixing efficiency in the ocean. *Annu. Rev. Mar. Sci.*, **10**, 443–473, https://doi.org/10.1146/annurev-marine-121916-063643.

Hebert, D., and J. Moum, 1994: Decay of a near-inertial wave. *J. Phys. Oceanogr.*, **24**, 2334–2351, https://doi.org/10.1175/1520-0485(1994)024<2334:DOANIW>2.0.CO;2.

Henyey, F. S., J. Wright, and S. M. Flatté, 1986: Energy and action flow through the internal wave field: An Eikonal approach. *J. Geophys. Res.*, **91**, 8487–8495, https://doi.org/10.1029/JC091iC07p08487.

Holbrook, W. S., I. Fer, R. W. Schmitt, D. Lizarralde, J. M. Klymak, L. C. Helfrich, and R. Kubichek, 2013: Estimating oceanic turbulence dissipation from seismic images. *J. Atmos. Oceanic Technol.*, **30**, 1767–1788, https://doi.org/10.1175/JTECH-D-12-00140.1.

Itsweire, E., T. Osborn, and T. Stanton, 1989: Horizontal distribution and characteristics of shear layers in the seasonal thermocline. *J. Phys. Oceanogr.*, **19**, 301–320, https://doi.org/10.1175/1520-0485(1989)019,0301:HDACOS.2.0.CO;2.

Jaeger, G. S., J. MacKinnon, A. Lucas, E. Shroyer, J. Nash, A. Tandon, J. Farrar, and A. Mahadevan, 2020: How spice is stirred in the Bay of Bengal. *J. Phys. Oceanogr.*, **50**, 2669–2688, https://doi.org/10.1175/JPO-D-19-0077.1.

Katz, E. J., 1973: Profile of an isopycnal surface in the main thermocline of the Sargasso Sea. *J. Phys. Oceanogr.*, **3**, 448–457, https://doi.org/10.1175/1520-0485(1973)003<0448:POAISI>2.0.CO;2.

Klymak, J. M., and J. N. Moum, 2007: Oceanic isopycnal slope spectra. Part II: Turbulence. *J. Phys. Oceanogr.*, **37**, 1232–1245, https://doi.org/10.1175/JPO3074.1.

——, W. Crawford, M. H. Alford, J. A. MacKinnon, and R. Pinkel, 2015: Along-isopycnal variability of spice in the North Pacific. *J. Geophys. Res. Oceans*, **120**, 2287–2307, https://doi.org/10.1002/2013JC009421.

Kunze, E., 1993: Submesoscale dynamics near a seamount. Part II: The partition of energy between internal waves and geostrophy. *J. Phys. Oceanogr.*, **23**, 2589–2601, https://doi.org/10.1175/1520-0485(1993)023<2589:SDNASP>2.0.CO;2.

——, 2017: Internal–wave–driven mixing: Global geography and budgets. *J. Phys. Oceanogr.*, **47**, 1325–1345, https://doi.org/10.1175/JPO-D-16-0141.1.

——, 2019: A unified model spectrum for anisotropic stratified and isotropic turbulence in the ocean and atmosphere. *J. Phys. Oceanogr.*, **49**, 385–407, https://doi.org/10.1175/JPO-D-18-0092.1.

——, E. Firing, J. M. Hummon, T. K. Chereskin, and A. M. Thurnherr, 2006: Global abyssal mixing inferred from lowered ADCP shear and CTD strain profiles. *J. Phys. Oceanogr.*, **36**, 1553–1576, https://doi.org/10.1175/JPO2926.1.

——, J. Klymak, R.-C. Lien, R. Ferrari, C. Lee, M. Sundermeyer, and L. Goodman, 2015: Submesoscale water-mass spectra in the Sargasso Sea. *J. Phys. Oceanogr.*, **45**, 1325–1338, https://doi.org/10.1175/JPO-D-14-0108.1.

Lien, R.-C., and P. Müller, 1992: Consistency relations for gravity and vortical modes in the ocean. *Deep-Sea Res.*, **39A**, 1595–1612, https://doi.org/10.1016/0198-0149(92)90050-4.

——, and T. B. Sanford, 2019: Small-scale potential vorticity in the upper-ocean thermocline. *J. Phys. Oceanogr.*, **49**, 1845–1872, https://doi.org/10.1175/JPO-D-18-0052.1.

——, ——, J. A. Carlson, and J. H. Dunlap, 2016: Autonomous microstructure EM-APEX floats. *Methods Oceanogr.*, **17**, 282–295, https://doi.org/10.1016/j.mio.2016.09.003.

Lindborg, E., 2005: The effect of rotation on the mesoscale energy cascade in the free atmosphere. *Geophys. Res. Lett.*, **32**, L01809, https://doi.org/10.1029/2004GL021319.

——, 2006: The energy cascade in a strongly stratified fluid. *J. Fluid Mech.*, **550**, 207–242, https://doi.org/10.1017/S0022112005008128.

——, and J. Y. Cho, 2000: Determining the cascade of passive scalar variance in the lower stratosphere. *Phys. Rev. Lett.*, **85**, 5663–5666, https://doi.org/10.1103/PhysRevLett.85.5663.

Marmorino, G., 1987: Observations of small-scale mixing processes in the seasonal thermocline. Part II: Wave breaking. *J. Phys. Oceanogr.*, **17**, 1348–1355, https://doi.org/10.1175/1520-0485(1987)017<1348:OOSSMP>2.0.CO;2.

——, and C. Trump, 1991: "Turbulent mixing" induced by upgoing near-inertial waves in the seasonal thermocline of the Norwegian Sea. *J. Geophys. Res.*, **96**, 7137–7143, https://doi.org/10.1029/91JC00084.

——, L. Rosenblum, J. Dugan, and C. Shen, 1985: Temperature fine-structure patches near an upper ocean density front. *J. Geophys. Res.*, **90**, 11 799–11 810, https://doi.org/10.1029/JC090iC06p11799.

——, ——, and C. Trump, 1987: Fine-scale temperature variability: The influence of near-inertial waves. *J. Geophys. Res.*, **92**, 13 049–13 062, https://doi.org/10.1029/JC092iC12p13049.

McComas, C. H., and P. Müller, 1981: The dynamic balance of internal waves. *J. Phys. Oceanogr.*, **11**, 970–986, https://doi.org/10.1175/1520-0485(1981)011<0970:TDBOIW>2.0.CO;2.

McKean, R. S., and T. E. Ewart, 1974: Temperature spectra in the deep ocean off Hawaii. *J. Phys. Oceanogr.*, **4**, 191–199, https://doi.org/10.1175/1520-0485(1974)004<0191:TSITDO>2.0.CO;2.

Molemaker, M. J., J. C. McWilliams, and X. Capet, 2010: Balanced and unbalanced routes to dissipation in an equilibrated Eady flow. *J. Fluid Mech.*, **654**, 35–63, https://doi.org/10.1017/S0022112009993272.

Müller, P., 1984: Small-scale vortical motions. *Internal Gravity Waves and Small Scale Turbulence: Proc. of the Second 'Aha Huliko'a Hawaiian Winter Workshop.* Honolulu, HI, Hawaii Institute of Geophysics, 249–262.

Nastrom, G., and K. S. Gage, 1985: A climatology of atmospheric wavenumber spectra of wind and temperature observed by commercial aircraft. *J. Atmos. Sci.*, **42**, 950–960, https://doi.org/10.1175/1520-0469(1985)042<0950:ACOAWS>2.0.CO;2.

Osborn, T., 1980: Estimates of the local rate of vertical diffusion from dissipation measurements. *J. Phys. Oceanogr.*, **10**, 83–89. https://doi.org/10.1175/1520-0485(1980)010<0083:EOTLRO>2.0.CO;2

Ozmidov, R. V., 1965: On the turbulent exchange in a stably stratified ocean. *Atmos. Oceanic Phys.*, **1**, 861–871.

Peters, H., M. C. Gregg, and T. B. Sanford, 1995: On the parameterization of equatorial turbulence: Effect of fine–scale variations below the range of the diurnal cycle. *J. Geophys. Res.*, **100**, 18 333–18 348, https://doi.org/10.1029/95JC01513.

Pinkel, R., 2014: Vortical and internal wave shear and strain. *J. Phys. Oceanogr.*, **44**, 2070–2092, https://doi.org/10.1175/JPO-D-13-090.1.

——, J. Sherman, J. Smith, and S. Anderson, 1991: Strain: Observations of the vertical gradient of isopycnal vertical displacement. *J. Phys. Oceanogr.*, **21**, 527–540, https://doi.org/10.1175/1520-0485(1991)021<0527:SOOTVG>2.0.CO;2.

Poje, A. C., T. M. Özgökmen, D. J. Bogucki, and A. Kirwan, 2017: Evidence of a forward energy cascade and Kolmogorov self-similarity in submesoscale ocean surface drifter observations. *Phys. Fluids*, **29**, 020701, https://doi.org/10.1063/1.4974331.

Polzin, K. L., J. M. Toole, and R. W. Schmitt, 1995: Finescale parameterizations of turbulent dissipation. *J. Phys. Oceanogr.*, **25**, 306–328, https://doi.org/10.1175/1520-0485(1995)025<0306:FPOTD>2.0.CO;2.

——, E. Kunze, J. Toole, and R. Schmitt, 2003: The partition of fine scale energy into internal waves and subinertial motions. *J. Phys. Oceanogr.*, **33**, 234–248, https:/doi.org/10.1175/1520-0485(2003)033<0234:TPOFEI>2.0.CO;2.

Riedel, K. S., and A. Sidorenko, 1995: Minimum bias multiple taper spectral estimation. *IEEE Trans. Sig. Proc.*, **43**, 188–195, https://doi.org/10.1109/78.365298.

Riley, J. J., and S. M. DeBruynkops, 2003: Dynamics of turbulence strongly influenced by buoyancy. *Phys. Fluids*, **15**, 2047–2059, https://doi.org/10.1063/1.1578077.

——, and E. Lindborg, 2008: Stratified turbulence: A possible interpretation of some geophysical turbulence measurements. *J. Atmos. Sci.*, **65**, 2416–2424, https://doi.org/10.1175/2007JAS2455.1.

Rosenblum, L., and G. Marmorino, 1990: Statistics of mixing patches observed in the Sargasso Sea. *J. Geophys. Res.*, **95**, 5349–5357, https://doi.org/10.1029/JC095iC04p05349.

Ruddick, B., and K. Richards, 2003: Oceanic thermohaline intrusions: Observations. *Prog. Oceanogr.*, **56**, 499–527, https://doi.org/10.1016/S0079-6611(03)00028-4.

——, A. Anis, and K. Thompson, 2000: Maximum likelihood spectral fitting: The Batchelor spectrum. *J. Atmos. Oceanic Technol.*, **17**, 1541–1555, https://doi.org/10.1175/1520-0426(2000)017<1541:MLSFTB>2.0.CO;2.

Samelson, R. M., and C. A. Paulson, 1988: Towed thermistor chain observations of fronts in the subtropical North Pacific. *J. Geophys. Res.*, **93**, 2237–2246, https://doi.org/10.1029/JC093iC03p02237.

Sanford, T. B., R. G. Driver, and J. H. Dunlap, 1985: An acoustic Doppler and electromagnetic velocity profiler. *J. Atmos. Oceanic Technol.*, **2**, 110–124, https://doi.org/10.1175/1520-0426(1985)002<0110:AADAEV>2.0.CO;2.

——, J. H. Dunlap, J. A. Carlson, D. C. Webb, and J. B. Girton, 2005: Autonomous velocity and density profiler: EM-APEX. *Proc. of the IEEE/OES Eighth Working Conf. on Current Measurement Technology*, Southampton, United Kingdom, Institute of Electrical and Electronics Engineers, 152–156, https://doi.org/10.1109/CCM.2005.1506361.

Scott, R., 2006: Local and nonlocal advection of a passive scalar. *Phys. Fluids*, **18**, 116601, https://doi.org/10.1063/1.2375020.

Sheen, K., N. White, and R. Hobbs, 2009: Estimating mixing rates from seismic images of oceanic structure. *Geophys. Res. Lett.*, **36**, L00D04, https://doi.org/10.1029/2009GL040106.

Smith, K. S., and R. Ferrari, 2009: The production and dissipation of compensated thermohaline variance by mesoscale stirring. *J. Phys. Oceanogr.*, **39**, 2477–2501, https://doi.org/10.1175/2009JPO4103.1.

Smith, S. A., D. C. Fritts, and T. E. Vanzandt, 1987: Evidence for a saturated spectrum of atmospheric gravity waves. *J. Atmos. Sci.*, **44**, 1404–1410, https://doi.org/10.1175/1520-0469(1987)044<1404:EFASSO>2.0.CO;2.

Stern, M. E., 1975: *Ocean Circulation Physics*. Academic Press, 246 pp.

Tang, Q., S. P. Gulick, J. Sun, L. Sun, and Z. Jing, 2020: Submesoscale features and turbulent mixing of an oblique anticyclonic eddy in the Gulf of Alaska investigated by marine seismic survey data. *J. Geophys. Res. Oceans*, **125**, e2019JC015393, https://doi.org/10.1029/2019JC015393.

——, Z. Jing, J. Lin, and J. Sun, 2021: Diapycnal mixing in the subthermocline of the Mariana Ridge from high-resolution seismic images. *J. Phys. Oceanogr.*, **51**, 1283–1300, https://doi.org/10.1175/JPO-D-20-0120.1.

Waite, M. L., and P. Bartello, 2004: Stratified turbulence dominated by vortical motion. *J. Fluid Mech.*, **517**, 281–308, https://doi.org/10.1017/S0022112004000977.

Whalen, C., L. Talley, and J. MacKinnon, 2012: Spatial and temporal variability of global ocean mixing inferred from Argo profiles. *Geophys. Res. Lett.*, **39**, L18612, https://doi.org/10.1029/2012GL053196.